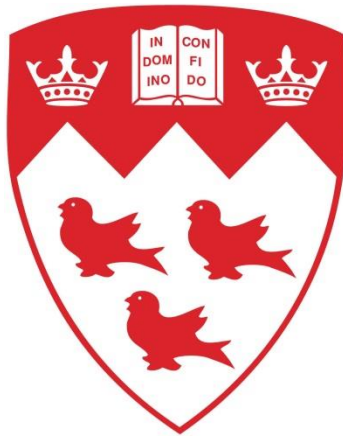


# Porous graded biomaterial for a tibial-knee implant with minimum bone resorption and bone-implant interface micromotion

Amirmohammad Rahimizadeh

Department of Mechanical Engineering



A thesis submitted to McGill University in partial fulfillment of the requirements for the degree of Master of Engineering.

August 2017

© Amirmohammad Rahimizadeh, 2017

## **Acknowledgments**

I would like to express my sincere gratitude to my supervisor Professor Damiano Pasini for his continuous support and technical guidance throughout my Master's study. His patience, motivation and immense knowledge helped me in all the time. The door to Prof. Pasini's office was always open whenever I ran into a trouble spot or had a question about my research or writing. I would like to thank you for giving me the great opportunity of being a part of your team.

I would also like to express the deepest appreciation to my family and friends for their support and encouragement during my study. My parents, Hossein and Marzieh, receive my deepest gratitude and love for their dedication and many years of support that provided the foundation of this work. I dedicate this thesis to them.

## Abstract

Numerous patients undergoing total knee arthroplasty (TKA) suffer from post-operative complications associated with TKA, namely end of stem pain and aseptic loosening. The mechanical mismatch between the implant and the surrounding bone has been identified as one major cause for implant failure. After primary TKA, the mechanical bio-incompatibility of the implant with the surrounding bone tissue results in bone resorption, which leads to revision surgery. Revision surgeries are generally more complex and often associated with a lower chance of success when compared to primary TKA. Excessive micromotion at the bone-implant interface raised from periprosthetic bone resorption is attributed to the end-of-stem pain following primary TKA. The incidence of end-of-stem pain is documented to be 7% for patients undergoing primary TKA. In revision surgery, furthermore, end-of-stem pain affects 16% of patients.

Substantial amount of work exists in literature attempting to improve the design of knee implants for enhanced performance and reduced clinical problems. Elastic property tailoring in hip stems was recognized already in the 1990s as a promising mean to reduce bone resorption. Whereas those studies focused on the use of functionally graded solid materials, only recently porous materials with tailored cellular architecture have been successfully exploited to create locally controlled compliant implants with reduced bone resorption.

In this thesis, we propose a fully porous tibial knee implant which features an optimally customized lattice microarchitecture. Its cellular microstructure contributes to a notable increase of the implant compliance, which leads to a simultaneous minimization of bone resorption and interface micromotion. A tetrahedron based cell unit is used as a building block for the lattice microarchitecture of the implant and its mechanical properties are characterized via Asymptotic Homogenization (AH) theory. A scheme combining multiscale mechanics and topology optimization is employed to tailor the material distribution of the implant against fatigue failure.

The results show the amount of bone resorption around the graded lattice implant to be 25% lower than that around a conventional fully dense titanium implant currently in the market. In addition, an improved interface micromotion which is as low as 17  $\mu\text{m}$  and 22  $\mu\text{m}$  respectively during the gait cycle and deep bend, is guaranteed by the newly introduced implant, thereby

alleviating the post-operative end of stem pain which patients with current implants can suffer from.

## Abrégé

De nombreux patients soumis à une arthroplastie totale du genou (TKA) souffrent de complications post-opératoires associées à TKA, à savoir la fin de la douleur de la tige et le relâchement aseptique. L'incomparabilité mécanique entre l'implant et l'os environnant a été identifiée comme la principale cause de défaillance de l'implant. Après le TKA primaire, la bio-incompatibilité mécanique de l'implant avec le tissu osseux environnant entraîne une résorption osseuse, ce qui conduit à une chirurgie de révision. Les chirurgies de révision sont généralement plus complexes et souvent associées à une plus faible chance de succès par rapport à la TKA primaire. Une micromotion excessive à l'interface os-implant élevée à partir de la résorption osseuse de la periprotèse est attribuée à la douleur de fin de tige après TKA primaire. L'incidence de la douleur à la fin de la tige est documentée à 7% pour les patients soumis à une TKA primaire. En chirurgie de révision, en outre, la douleur à la fin de la tige affecte 16% des patients.

Il existe une quantité considérable de travail dans la littérature visant à améliorer la conception des implants au genou pour améliorer les performances et réduire les problèmes cliniques. L'adaptation élastique de la propriété dans les tiges de la hanche a déjà été reconnue dans les années 1990 comme un moyen prometteur de réduire la résorption osseuse. Alors que ces études ont porté sur l'utilisation de matériaux solides fonctionnellement classés, seuls des matériaux poreux récents avec une architecture cellulaire sur mesure ont été exploités avec succès pour créer des implants conformes contrôlés localement avec une résorption osseuse réduite. Dans cette thèse, nous proposons un implant de genou tibial entièrement poreux qui présente une microarchitecture en treillis personnalisée. Sa microstructure cellulaire contribue à une augmentation notable de la compliance de l'implant, ce qui conduit à une minimisation simultanée de la résorption osseuse et de la micromotion de l'interface. Une unité de cellules à base de tétraèdre est utilisée comme élément de construction pour la microarchitecture en réseau de l'implant et ses propriétés mécaniques sont caractérisées par une théorie de l'homogénéisation asymptotique (AH). Un schéma combinant l'optimisation de la topologie et la mécanique multiscalaire est utilisé pour adapter la distribution matérielle de l'implant contre une panne de fatigue.

Les résultats montrent que la quantité de résorption osseuse autour de l'implant en treillis gradué est inférieure de 25% à celle d'un implant de titane classique entièrement dense actuellement sur

le marché. De plus, une micromotion d'interface améliorée de 17  $\mu\text{m}$  et 22  $\mu\text{m}$  respectivement pendant le cycle de marche et le virage profond est garantie par l'implant nouvellement introduit, ce qui atténue l'extrémité post-opératoire de la douleur de la tige que les patients présentant des implants actuels peuvent souffrir de.

# Table of Contents

<b>ACKNOWLEDGMENTS .....</b>	<b>II</b>
<b>CHAPTER 1: INTRODUCTION.....</b>	<b>1</b>
1.1 KNEE JOINT .....	1
1.2 BONE STRUCTURE OF KNEE JOINT.....	4
1.2.1 Femur.....	4
1.2.2 Tibia.....	5
1.2.3 Patella.....	7
1.2.4 Meniscus .....	8
1.3 TOTAL KNEE ARTHROPLASTY .....	9
1.3.1 Knee Prosthesis.....	10
1.3.2 Knee Implants Bearing Models.....	13
1.3.3 Cemented and Cementless Implants.....	14
1.3.4 Clinical Outcome of TKA.....	15
1.4 THESIS OBJECTIVE .....	19
1.5 THESIS ORGANIZATION.....	20
<b>CHAPTER 2: THEORY AND METHODS .....</b>	<b>21</b>
2.1 INTRODUCTION.....	21
2.2 METHODOLOGY .....	21
2.3 FINITE ELEMENT MODEL .....	23
2.4 HOMOGENIZED MECHANICAL PROPERTIES.....	27
2.4.1 Homogenization Techniques.....	27
2.4.2 Elastic properties of unit cell.....	29
2.4.3 Fatigue properties.....	31
2.5 CONCLUSION .....	32
<b>CHAPTER 3: TOPOLOGY OPTIMIZATION ALGORITHM .....</b>	<b>34</b>
3.1 CLASSICAL TOPOLOGY OPTIMIZATION.....	34
3.2 OPTIMIZATION METHODS .....	36
3.2.1 Optimality criteria method.....	36
3.2.2 Method of Moving Asymptotes.....	38
3.3 NUMERICAL PROBLEMS IN TOPOLOGY OPTIMIZATION.....	39
3.4 OPTIMIZATION SCHEME .....	40
3.4.1 Problem formulation.....	41
3.4.2 Derivation of the stiffness tensor for the implant internal microstructure.....	43
3.5 CONCLUSION .....	46
<b>CHAPTER 4: RESULTS AND DISCUSSION.....</b>	<b>47</b>
4.1 INTRODUCTION.....	47
4.2 IMPLANT ARCHITECTURE .....	47
4.3 IMPLANT MICROMOTION .....	48
4.4 BONE RESORPTION .....	52
4.5 CONCLUSIONS .....	56

CHAPTER 5: FINAL REMARKS AND FUTURE WORK.....	58
5.1 SUMMARY .....	58
5.2 FUTURE WORK.....	59
REFERENCES.....	61
APPENDICES .....	71
APPENDIX A: ASSIGNING BONE MATERIAL PROPERTIES USING COMPUTED TOMOGRAPHY (CT) DATA .....	71
APPENDIX B: FILTER DENSITY FUNCTION .....	73
APPENDIX C: CONVERGENCE PLOT OF THE TOPOLOGY OPTIMIZATION SCHEME ....	74



## List of Tables

Table 1: Loading conditions used in this study. F1, F2 and F3 act in the medio-lateral, vertical and posterior-anterior directions respectively. M1, M2 and M3 act in the sagittal, horizontal and frontal plane of the tibiae, as shown at the right top corner in Fig 17. ....	27
--	----

## List of Figures

Figure 1: The anatomy of the knee joint. ....	2
Figure 2: The anatomy of bones forming the knee joint including femur and tibia. ....	3
Figure 3: Rotation mechanism of the femur over the tibia [6]. ....	4
Figure 4: Posterior (A), and anterior (B) view of proximal and distal end of femur[8] . ....	5
Figure 5: Anterior (A), and posterior (B) view of the tibia along with the proximal and distal condyles [9]. .....	6
Figure 6: Attachment of ligaments and meniscus at the tibial condyles [10]. ....	7
Figure 7: Anterior (A) vs. lateral (B) view of the patella at the knee joint [12]. ....	8
Figure 8: Superior view of menisci at the knee joint [5]. ....	9
Figure 9: Process of proximal tibia resection. The tibia is resected at 90° degrees to its mechanical axis and 10mm beneath the top surface [5]. ....	10
Figure 10: The femoral component of a knee prosthesis [16]. ....	11
Figure 11; The tibial component of a knee prosthesis [19]. ....	12
Figure 12: The patellar component of a knee prosthesis [20]. ....	12
Figure 13: Fixed-bearing knee implant (A) vs. rotating bearing knee implant (B) under femoral axial rotation [21]. ....	13
Figure 14; Mobile-bearing implants provide a larger contact area than fixed-bearing implants thus resulting in lower contact stress. [24] ....	14
Figure 15; Flow chart illustrating the analysis and design scheme used to develop a graded cellular knee implant minimizing bone resorption and interface micromotion. ....	23
Figure 16: CT scan data used to create the solid model of the tibia along with the dimensions of the tibia and tibial knee implant in mm. Frontal view of the tibia (a), sagittal view of the tibia (b), Frontal view of the implant (c), sagittal view of the implant (c). ....	24
Figure 17: 3D finite element model of the intact tibiae (a), and implanted prosthesis (b). ....	26
Figure 18: Common cell topologies used to generate lattice structures [25]. ....	28
Figure 19: (A) Effective elastic and (B) effective strength properties of Tetrahedron based lattice as a function of relative density. Effective elastic properties and yield strengths normalized with respect	

to elastic properties and yield strengths of bulk material. Only three independent elastic constants are necessary for the tetrahedron-based cell which is orthotropic and has 3 planes of symmetry:

(Young's modulus),  $G_{xy}$  (Shear modulus) and  $\nu_{yz}$  (Poisson's ratio).  $\sigma_{xx}$ ,  $\sigma_{xy}$  and  $\sigma_{bxy}$  refer to uniaxial, shear and biaxial strength respectively. Values of  $\rho$  above 0.8 are dismissed due to cell topology degeneration..... 31

Figure 20: The initial (left) and final (right) designs of sizing (a), shape (b) and topology optimization (c) [107]...... 35

Figure 21: Optimum topology obtained for a mesh of (a) 2700, (b) 2800 and (c) 17200 elements. As the number of elements increase and mesh refines, the issue of mesh dependency leads to more holes in the optimum topology [63]. ..... 39

Figure 22: A cantilever beam featuring a poor optimum topology as a result of checkerboard pattern topology [122]...... 40

Figure 23: : (a) Von-Mises stress distribution; (b) optimum relative density distribution to ensure adequate fatigue resistance against daily cyclic loads; (c) graded cellular implant with tailored porosity in the stem ranging 0.3-0.7. A thin solid exterior (shown only partially in the figure) coats the stem, a clinically recommended feature introduced to ease implant removal at the time of revision surgery; (d) internal architecture of the tibial implant, where the thin shell is here omitted for a global visualization of the whole internal microstructure. .... 48

Figure 24: Interface micromotion distribution at 30% of gait cycle for a fully dense titanium implant (a), cellular implant with uniform relative density of 60% (b), and graded cellular implant (c). SA: surface area of the prosthesis. .... 50

Figure 25: Interface micromotion distribution at deep bend for a fully dense titanium implant (a), cellular implant with uniform relative density of 60% (b), and a graded cellular implant (c). SA: surface area of the prosthesis. .... 51

Figure 26: Relative distribution of interface micromotion around the stem surface with respect to the fully solid implant. % values are shown at the distal and mid regions along the stem length for 30% of gait cycle (a), and deep bend (b). .... 52

Figure 27: Distribution of bone resorption in knee prosthesis around (a) fully dense titanium implant; (b) cellular implant with uniform relative density of 60%; and (c) graded cellular implant. L: Lateral, M: Medial, A: Anterior, P: Posterior, AL: Anterolateral, AM: Anteromedial. .... 54

Figure 28: Percentage of bone resorption with respect to a fully solid tibial implant here taken as a baseline for (i) graded cellular implant, and (ii) uniform cellular implant with relative density of 0.6 . .... 55

## Chapter 1: Introduction

This chapter presents a brief introduction of the concepts involved in the context of this thesis. The first subsection describes the anatomy of the knee joint as well as the muscles and ligaments forming the knee joint. The second subsection describes the structure and material of the tibial knee implants currently in use, and discusses their functionality and limitations.

### 1.1 Knee Joint

The knee joint is one of the most studied joints in the human body. It serves an important role in the stability and support of body weight during daily activities. The numerous ligamentous attachments associated with the muscles crossing the joint enable the joint stability and mobility functions that allow the knee to withstand compressive forces up to six times of the body weight.

The knee consists of two distinct articulations placed within a single joint capsule and sharing the same articular cavity: the tibiofemoral joint, which is the articular surface between the distal end of the femur and the proximal tibia; and the patellofemoral joint, which is the articular surface between the posterior patella and the femur [1, 2]. As shown in Figure 1, the attachment of three main bones – the distal end of the femur, the proximal end of the tibia, and the patella – enables the knee to resist the heavy loads that might exceed six times the body weight. Numerous soft tissues, namely the ligaments, menisci, and tendons, enable the knee joint to reconcile the two antagonistic features of mobility and stability. The ligaments and menisci provide static stability, and the muscles and tendons offer dynamic stability. The anatomical fitting of the articular surface to the articular capsule (i.e., the topology of the articular surfaces that is associated with ligaments and cartilages) provides stabilizing capacity to the joint. Various muscles and their tendons form the dynamic stabilizers of the knee [2-4].

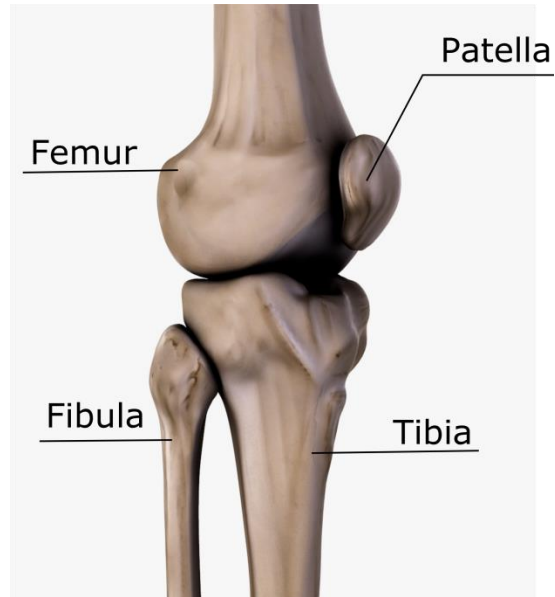


*Figure 1: The anatomy of the knee joint.*

The anatomy of the distal femur and the proximal tibia are shown in Figure 2. As can be seen, the condyles are convex in both planes. The medial condyle extends distally more than the lateral condyle, which contributes to the Varus-Valgus movements and prevents the patella from sliding. During flexion and extension, the tibia and patella act as one single structure with respect to the femur [5]. The anteroposterior elevation between the tibial condyles resembles the femoral intercondylar notch. The surface of the anteriorly projected tibial condyles corresponds to the articular surface of the patella and is relatively compatible with that of the femur [5].

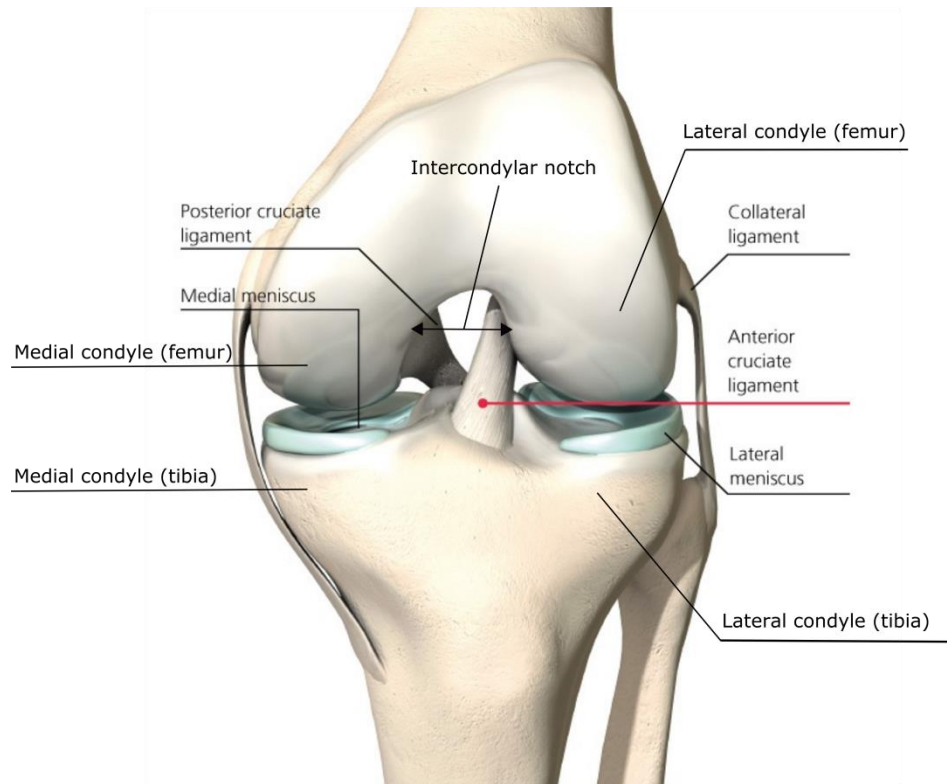


*Figure 2: The anatomy of bones forming the knee joint including femur and tibia.*

Figure 3 shows the mechanism of the femur rotation over the tibiofemoral articular surface. As can be observed, the femur acts like a wheel over the tibia, in that the medial and lateral condyles are the main components of the wheel, and the intercondylar notch is the junction between them. The main movement of the knee is flexion-extension. Secondary movements – i.e., internal and external rotation of the tibia relative to the femur – are feasible only when the knee is flexed. During the flexion-extension movement, the knee can be treated as a hinged joint, wherein the articular surface of the femur rolls over the tibial surface. The distal end of the femur can be treated as a double wheel that rotates in two perpendicular planes. In the case of large flexion, the quadriceps mechanism of the knee joint moves the patella anterior relative to the center of rotation of the knee.

## 6 Degrees of Motion present in the Human Knee

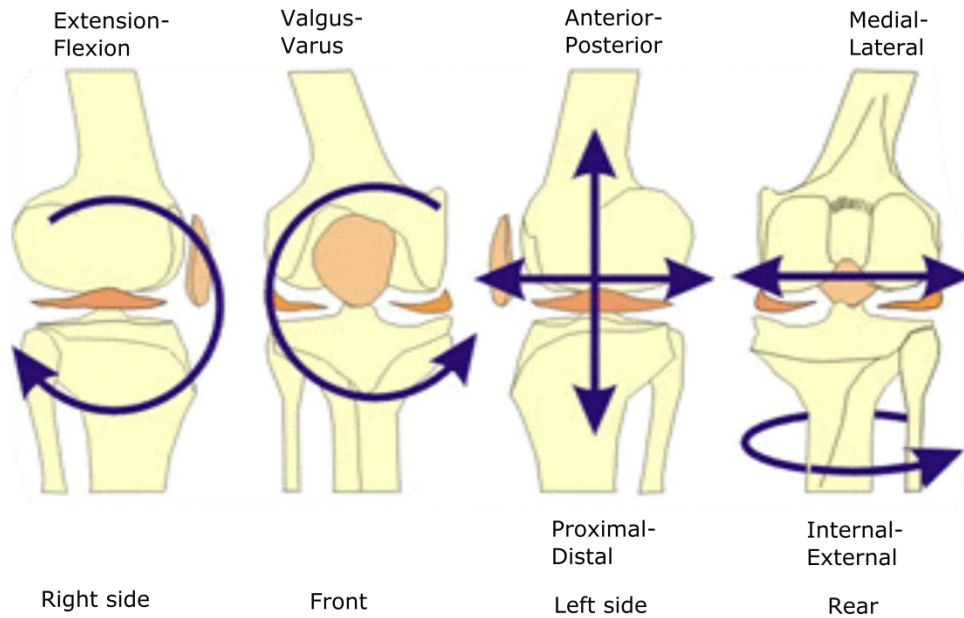


Figure 3: Rotation mechanism of the femur over the tibia [6].

### 1.2 Bone Structure of Knee Joint

The knee joint consists of three bones – femur, tibia, and patella – all of which are enclosed in a joint capsule.

#### 1.2.1 Femur

The thighbone (femur) is the longest and strongest bone in the human body. The high strength of the femur serves to withstand the large forces resulting from daily activities [1, 4, 7]. The femur is connected to the tibia through the knee joint, which transfers loads to the tibia and then to the ground.

As can be observed in Figure 4, on the proximal end the femur features a smooth, spherical component known as the head of the femur. The head of the femur is connected to the pelvis through a ball-socket joint with the cup-shaped acetabulum of the hip bone. The ball-socket joint allows rotation in any direction and contributes to the load transfer without friction. The long, straight portion of the femur is known as the femoral shaft. Two convex protrusions, the medial and the lateral femoral condyles, generate the distal end of the femur. The condyles are separated posteriorly through an intercondylar fossa. The condyles are joined anteriorly by the femoral trochlear groove or surface [1, 2]. The medial and lateral condyles of the femur

articulate with the medial and lateral condyles of the tibia to form the articular surfaces of the knee joint. The intercondylar fossa between the condyles provides space for the anterior cruciate ligament and posterior cruciate ligament (Figure 2) which facilitate stabilization of the knee along its anterior/posterior axis [5].

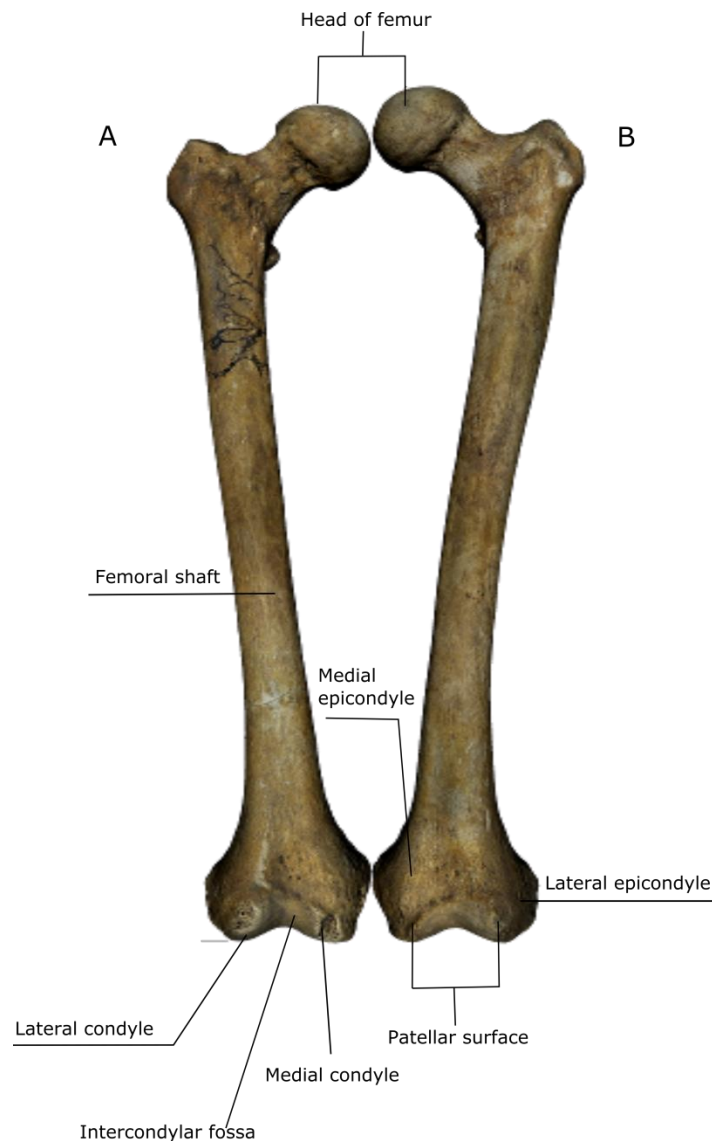


*Figure 4: Posterior (A), and anterior (B) view of proximal and distal end of femur[8].*

### **1.2.2 Tibia**

The tibia, or shinbone, is the second largest bone in the human body. It is located in the lower front portion of the leg, and articulates with the femur at the knee joint [1, 7]. As can be seen in Figure 5, the ankle is connected to the knee through two bones: the tibia and the fibula.

The fibula is smaller and thinner than the tibia. It plays a crucial role in stabilizing the ankle and supporting the muscles of the lower leg.

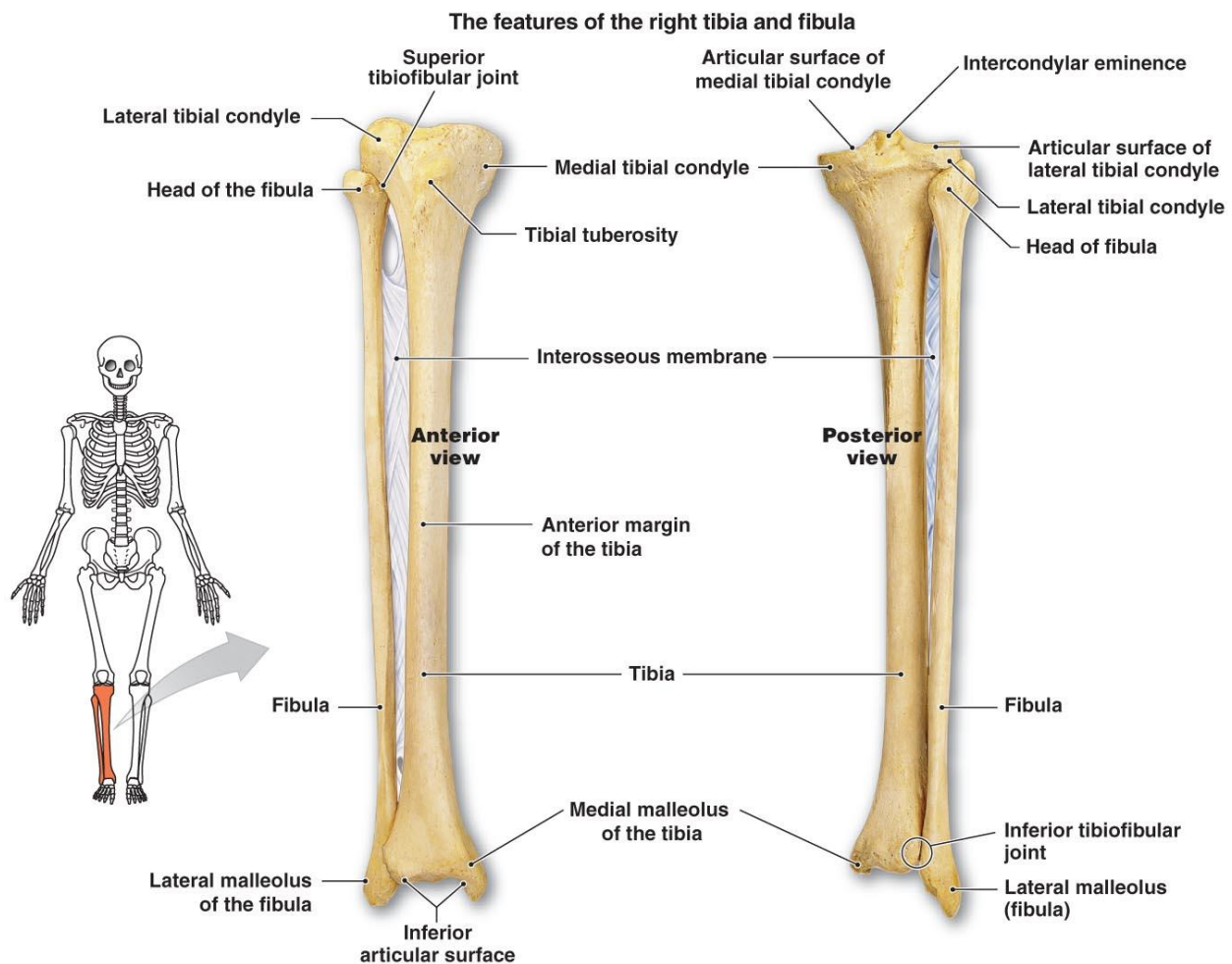
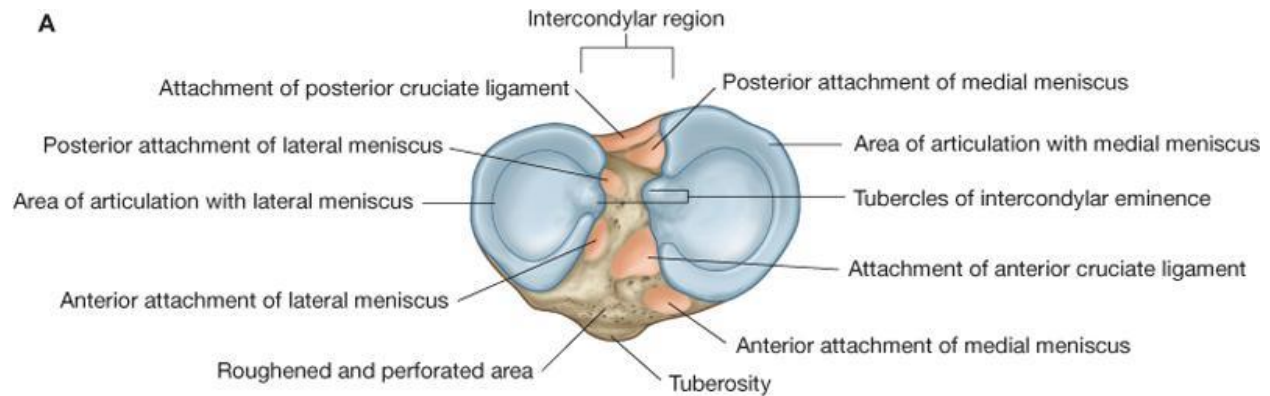


Figure 5: Anterior (A), and posterior (B) view of the tibia along with the proximal and distal condyles [9].

The large condyle of the tibia in the transverse plane provides high load-bearing capacity. An intercondylar region featuring a rough area and two bony spines separates the tibial condyles. The rough surface of the intercondylar region facilitates the attachment of the cruciate ligaments and menisci, as depicted in Figure 6[1, 2].





*Figure 6: Attachment of ligaments and meniscus at the tibial condyles [10].*

The central part of the tibial condyles articulates with the corresponding lower and posterior parts of the femur condyles and forms the knee joint. The exterior surfaces are in contact with the menisci. The articular surfaces of the tibial condyles and the intercondylar region form a ‘tibial plateau’ that articulates with the distal end of the femur and connects it to the proximal extremity of tibiae. Tibial plateaus are flat and slightly convex at the anterior and posterior margin, so as to slightly mismatch the convexity of the femoral condyle. Nevertheless, the meniscus offers a balance between the femur condyle and tibial plateau that leads to higher bone stability and facilitates the flexion and extension of the knee joint. During knee extension, the intercondylar fossa of the femur prevents the tibia from rotating with respect to the femur through lodging the intercondylar eminence of the tibia [1, 2, 7].

### **1.2.3 Patella**

The patella is a small bone located in front of the knee joint that articulates with the femur and protects the anterior articular surface of the knee joint from injuries. As Figure 7 shows, the patella has roughly a triangular shape that facilitates the attachment of the base to the quadriceps muscle. The upper third front of the patella is coarse, flat, and rough, characteristics that not only enable attachment to the tendon of the quadriceps but also contribute to the generation of new bone. Myriad vascular canaliculi in the middle third portion of the patella facilitate the generation of new, healthy bone [5].

The lower third part forms an apex and is the origin of the patellar ligament. The upper three quarters of the posterior surface articulate with the femur, whereas the lower part incorporates vascular canaliculi filled up by fatty tissue [11].

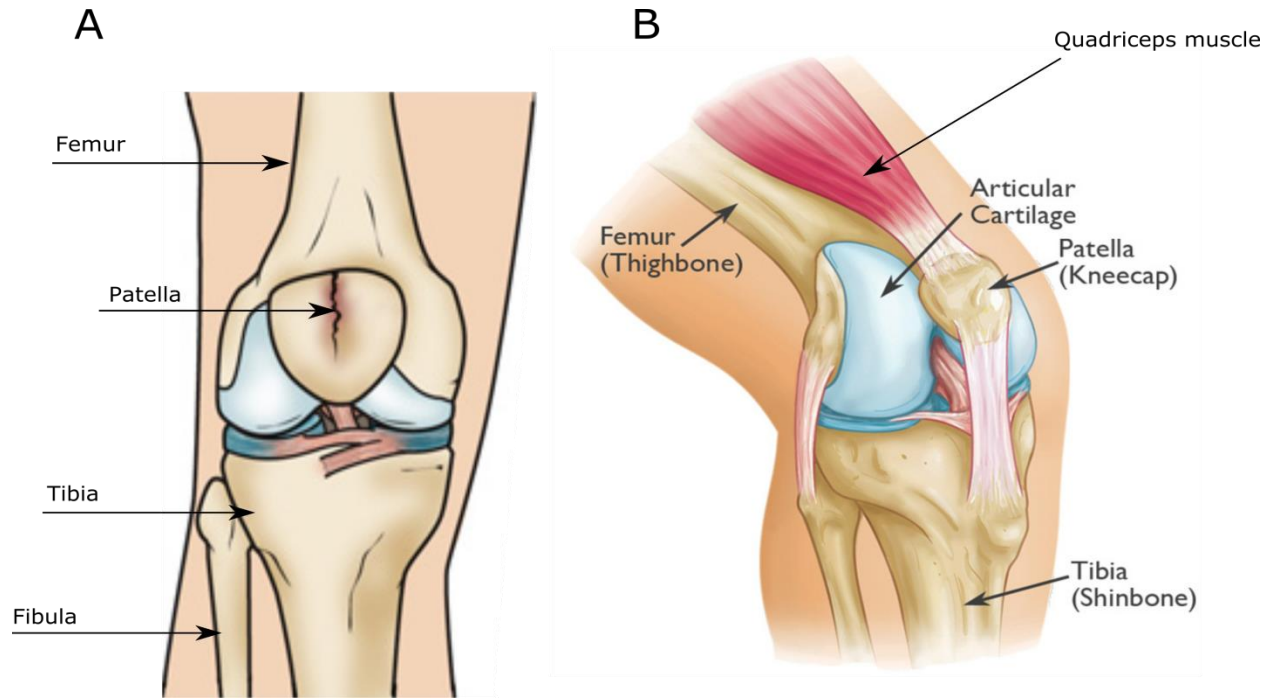
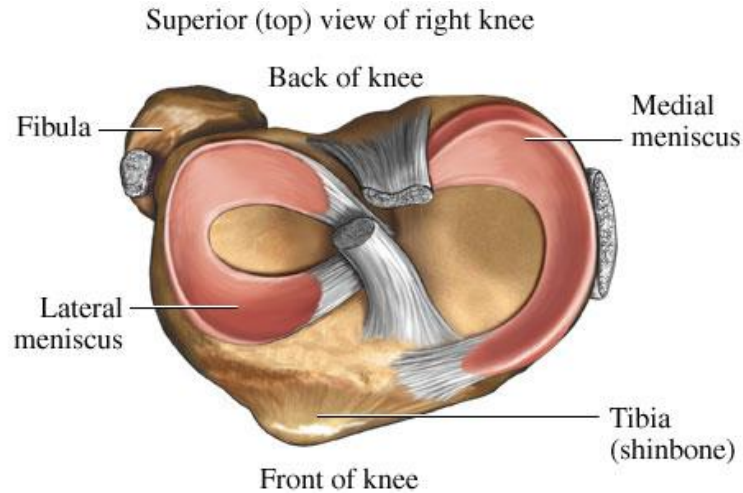


Figure 7: Anterior (A) vs. lateral (B) view of the patella at the knee joint [12].

#### 1.2.4 Meniscus

The menisci are semicircular fibrocartilage located on the articular surface of the tibial plateau (Figure 8). They serve as a shock absorber over the articular surface of the tibia and femur, and appropriately protect the knee joint and enhance the stability and performance of the joint by lubricating the articular surface. Moreover, they facilitate the articulation of the proximal tibia to the distal femur by providing a deep surface on the tibial plateau. The medial meniscus is relatively larger than the lateral one, and is thus more vulnerable to physical injuries. The blood supply to menisci decreases with age such that at the time of injury, it would not heal as quickly. A damaged meniscus should be treated since it plays a vital role in protecting the articular cartilage and it contributes to preventing knee arthrosis [1, 2].



*Figure 8: Superior view of menisci at the knee joint [5].*

### **1.3 Total Knee Arthroplasty**

Total Knee Arthroplasty (TKA) is considered one of the greatest achievements of orthopedic surgery. TKA allows the injured knee joint to be replaced with an implant featuring a macrogeometry similar to that of the knee joint anatomy. A TKA is usually required when a knee joint is fully or partially damaged due to disease or injury and can no longer function properly. The macro-geometry of the knee implants currently available on the market is similar to that of the knee joint, so as to facilitate the TKA operation and lead to a reasonable clinical outcome.

Figure 9 depicts the TKA process that is typically followed during surgery. In primary TKA, the surgeon makes an incision in the front of the knee to remove the patella and expose the joint that will host the implant. The proximal tibia and the distal femur are then accurately cut in a way that respectively matches the macrogeometry of the corresponding surface of the femoral and the tibial components. The proximal tibia is generally resected 10 mm beneath the top surface at 90° angle relative to its mechanical axis, which connects the center of the femoral head to the center of the ankle joint. Once the tibia is resected, the appropriate size of implant – that which provides the maximum stability and alignment – is determined by inserting various sizes of implant. Finally, the femoral and tibial components are placed and the tibial insert is snapped into the tibial component. The patella is then resurfaced with the patellar component in case of injury or resorption [13, 14].

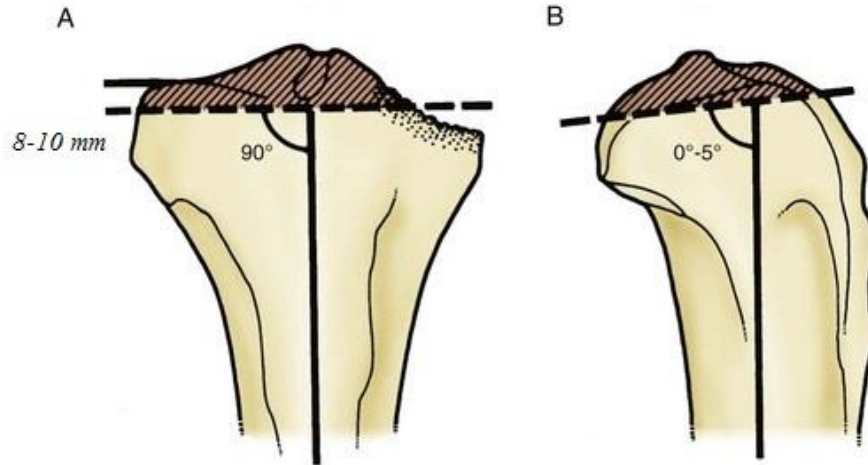
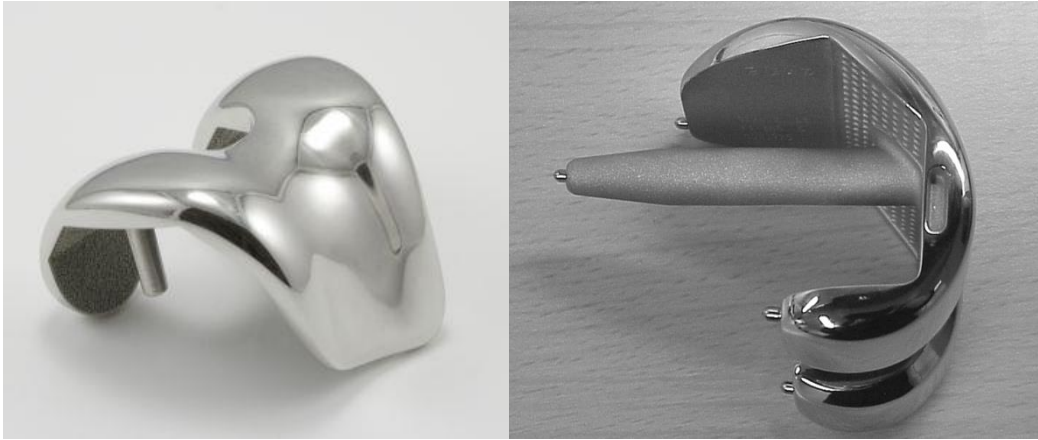


Figure 9: Process of proximal tibia resection. The tibia is resected at 90° degrees to its mechanical axis and 10mm beneath the top surface [5].

### 1.3.1 Knee Prosthesis

A knee implant consists of three main parts: tibial, femoral, and patellar. The knee replacement implants currently used in TKA are generally made of a fully solid material, such as titanium alloys or cobalt chrome (CoCr) and ultra-high molecular weight polyethylene. They also come with stems that provide more stability and enhance implant performance in the case of large bone degradation. Different designs and sizes of stems are available on the market. The appropriate implant size for each patient depends on bone-implant fixation, joint connection, and the amount of degraded bone.

The femoral component connects the distal end of the femur to the proximal end of the tibia and allows the weight bearing loads to be transferred from the femur to the tibia. As can be seen in Figure 10, the rounded geometry of the femoral components replicates the original shape of the distal femur and offers a large contact area at the articular surface between the femur and the tibia. Although the rounded coronal geometry of the femoral component limits the movement and rotation of the femur, it allows for varus-valgus movement of the knee joint that may occur in the normal gait cycle. Moreover, the femoral component consists of a single patella groove that fits finely with the patellar component, resulting in enhanced performance and function of the patellofemoral joint [15].



*Figure 10: The femoral component of a knee prosthesis [16].*

The tibial component replaces the proximal end of the tibia. As shown in Figure 11, the currently used tibial components are comprised of two single parts including the tibial tray and the stem. The tibial tray is placed over the resected tibia and is designed to transfer the weight bearing loads throughout the constituents. It features a cross-finned keel design that ensures sufficient strength to withstand the rotational forces. Moreover, a cross-finned keel design improves the stability and fixation of the tray. When the knee joint undergoes severe damage that results in a high amount of resorbed bone, an implant along with a long/short stem is required. The stem contributes to higher stability and facilitates the incidence of bone ingrowth by providing a larger contact area. The stems are usually made of metal alloys with a large variety in the macro-geometry [15]. Short stems are used in primary TKA, whereas long stems might be required in revision surgeries in order to increase fixation strength at the bone-implant interface [17].

The tibial insert is designed to be positioned over the tibial tray with the aim of providing additional stability. It also offers a high capacity for shock absorption and further improves the articulation surface between the tibial tray and the femoral component. As such, it serves as an artificial cartilage between the femoral component and the tibial baseplate [15]. The tibial inserts are generally made of UHMEPE (high-density polymer), which reduces the chance of prosthesis failure arising from wear. They also feature a central spine that engages in the corresponding intercondylar fossa of the femoral component and ensures adequate stabilization when posterior cruciate ligament is scarified [14, 18].

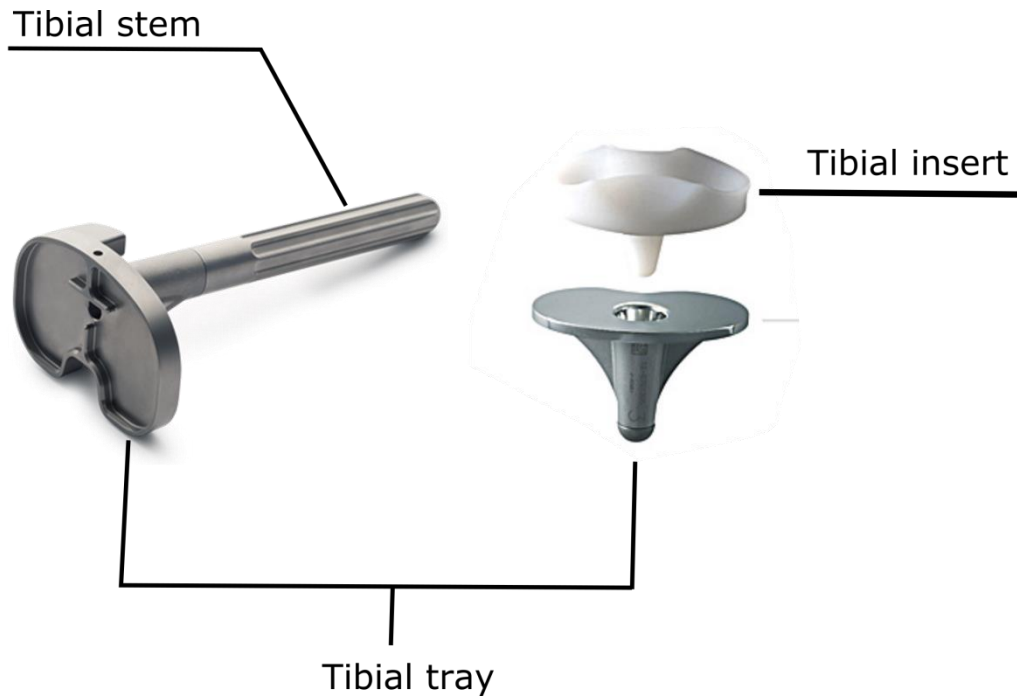


Figure 11; The tibial component of a knee prosthesis [19].

The patellar component (Figure 12) is generally made of UHMWPE and features a dome shape that replicates the macro-geometry of the patella. It articulates with the femoral component at the patellar groove with the aim of protecting the joint from damage. In some cases where the knee joint has not undergone severe damage, the patellar component is not replaced.

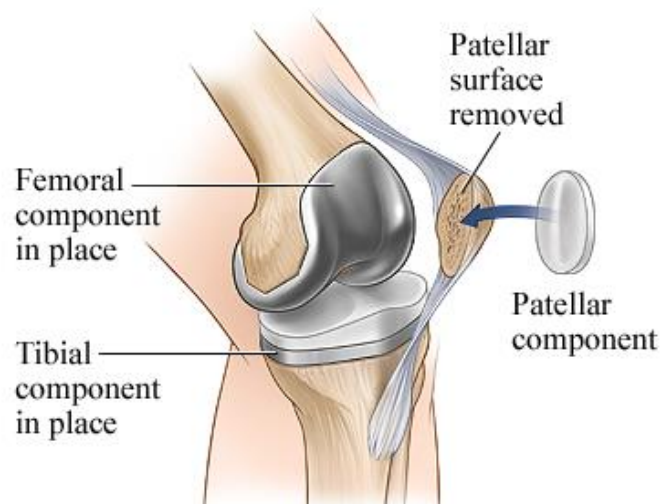


Figure 12: The patellar component of a knee prosthesis [20].



### 1.3.2 Knee Implants Bearing Models

Knee implants are divided into two main categories depending on their fundamental design principle, namely how the tibial insert is fixed to the tibial tray. These two models are fixed-bearing knees and mobile-bearing knees (Figure 13). Each fixation method allows for various types of knee arthroplasty such that the posterior cruciate ligament might be retained, scarified, or substituted.

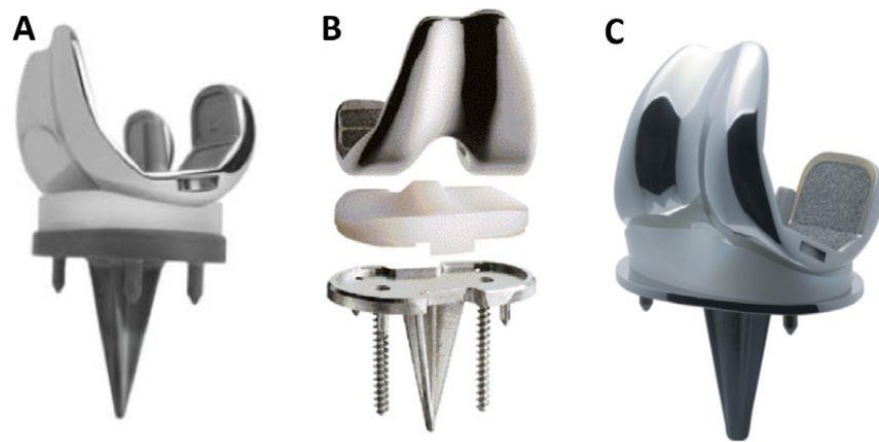


Figure 13: Fixed-bearing knee implant (A) vs. rotating bearing knee implant (B) under femoral axial rotation [21].

#### Fixed-Bearing Knee Implants

Fixed-bearing knee implants limit the movement of the tibial insert with respect to the tibial tray by locking the polyethylene tibial insert to the tray. This type of bearing is generally associated with implant loosening and polyethylene wear, which ultimately result in implant failure. Although a fixed-bearing prosthesis with a high-conformity bearing surface generates low contact stress values, high torque values at the bone-implant interface have been documented; these characteristics predispose the patient to component loosening. In addition, the issue of kinematic conflict between the low-stress articulation and the free rotation cannot be addressed by this type of knee bearing design [22, 23].

#### Mobile-Bearing Knee Implants

Mobile-bearing implants were first introduced with the goal of mitigating the incidence of polyethylene wear and component loosening. As shown in Figure 14, they enable geometrical congruity and mobility in the tibiofemoral bearing surface, which leads to low contact stress and constraint force, thus enhancing wear resistance. Mobile-bearing implants, furthermore, feature a

high conforming articular surface that can freely rotate in all different directions. This exciting characteristic can reasonably be expected to address the problem of kinematic conflict between low-stress articulation and free rotation [22, 23].

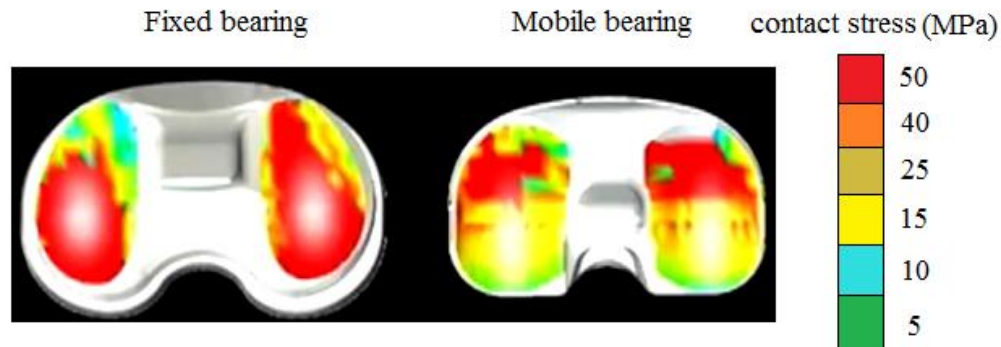


Figure 14; Mobile-bearing implants provide a larger contact area than fixed-bearing implants thus resulting in lower contact stress. [24]

### 1.3.3 Cemented and Cementless Implants

Knee implants are generally attached to the surrounding bone through two common types of fixation modes: cemented and cementless implants. The type of implant fixation is commonly selected according to the amount of resorbed bone, the patient's bone anatomy, and the bone quality. For instance, in the case of fragile bone, a cemented stem with the goal of providing additional stability at the bone-implant interface is desired. On the other hand, a press-fit fixation is preferred when bone resorption is not substantial and the bone can provide adequate stability and support at the bone-implant interface.

In cemented implants, a fast-drying bone cement is used to attach the implant to the surrounding bone. Although the high stiffness and strength of the cement ensure a stable and strong fixation at the bone-implant interface, the fatigue failure of the cement has recently been observed in young patients. The debris of the cement can irritate the surrounding soft tissue and result in inflammation. Another underlying complication associated with the use of cement is the risk of cement entering the blood stream, after which it often ends up in the lungs and threatens the patient's health [25].

An alternative to the cemented fixation was introduced in the mid-1970s. The implant was designed with a porous surface that would biologically attach to the bone tissue by allowing



bone ingrowth. In a cementless fixation, the rough surface of the implant stimulates the surrounding bone, facilitating osseointegration. Furthermore, a press-fit fixation provides long-term stability that can enhance the implant performance and reduce the probability of implant failure and revision surgery. In cementless implants, the dimension of the stem is identical to that of the reamer used to drill the hole through the tibia, which ensures a suitable fit between the bone and the implant [18, 25]. In the case of a high amount of resorbed bone, however, a cementless implant is not an appropriate option due to the limited incidence of bone ingrowth and thus inadequate bone support.

Porosity, pore size, interconnectivity between pores, and roughness of the implant surface have been identified as factors for bone formation that play an important role in the strength of the interface bonding [26-28]. A porous surface featuring interconnected pores facilitates vascularization and transportation of nutrients for bone cells that result in excessive osseointegration and bone ingrowth [25]. A rough implant surface ensures an initial stability required for bone ingrowth and mechanical fixation. Furthermore, surface microtexture and microporosity provide a larger area that contributes to greater bone formation. Besides this, microporosity of the implant surface facilitates ion exchange and bone-like apatite formation through dissolution and reprecipitation [25]. In a study by Bobyn et al. [29], a porous surface with a pore size ranging 50 to 400 microns has been demonstrated to provide the maximum possible fixation strength at the bone-implant interface. In another study by Bragdon et al. [30], the interplay between porosity and pore size for optimum bone ingrowth was investigated. They have reported that a mean pore size of  $P > 200 \mu\text{m}$  and a porosity of  $\phi > 40\%$  provide a desirable environment that maximizes the incidence of osseointegration.

#### **1.3.4 Clinical Outcome of TKA**

The success of TKA depends on myriad factors including patient-related factors, implant design, implant material and mechanical properties, appropriate sizing, accuracy of component alignment, and soft tissue balancing [18, 31, 32]. Although a partially successful TKA with a satisfactory clinical outcome may be achieved by properly selecting the implant, TKA is generally associated with several potential complications, namely aseptic loosening, bone resorption, end of stem pain, and implant fracture [18, 32, 33]. Patient-related factors, such as sickle cell anaemia [34], poor bone quality [34], and high body mass index [35] may also result

in implant failure predisposing the patient to infections and dislocation. A recent study in the US revealed that 60,355 patients who had undergone revision surgeries between 2005 and 2006 suffered from infection and implant loosening [5].

A significant amount of recent literature has attempted to improve the characteristics of the implants currently on the market, with the aim of decreasing the probability of implant failure and thus the likelihood of revision surgery. Despite their improved characteristics when compared to the implants of the late 1970s, existing knee stems feature homogeneous properties that limit their performance and fail to fulfill the complete set of mechanobiological requirements they are subjected to [36]. One of these is end-of-stem pain, which is experienced by 7% patients that undergo primary TKA. In revision surgery, despite the adoption of modified long stems, end-of-stem pain has been reported to affect as many as 19% of patients [37]. The etiology of this pain is most commonly attributed to the severe interface micromotion that develops between the stem tip and the surrounding native bone, a problem that results from the elastic modulus mismatch existing between them [38]. The second consequence of an elastic modulus mismatch between the tibial implant and the surrounding host bone is bone resorption secondary to stress shielding.

A significant incidence of end-of-stem pain has been documented for both fully cementless and fully cemented stems with stable fixation [39, 40]. In an experimental study by Barrack et al. [41], pain drawings were clinically used to assess the probability of end-of-stem pain in 16 patients receiving fully cemented stems and 50 patients with a fully cementless fixation. They found a 19% incidence of end-of-stem pain in patients with fully cemented stems and 14% incidence in knees with a press-fit, cementless stem. As an alternative, hybrid fixation of a stemmed tibial component has been proposed and has now become the standard of care. With this technique, the tibial plateau and the proximal metaphysis are cemented, whereas the stem is cementless and press-fit into the tibial diaphysis [42]. Nevertheless, although this type of fixation offers a lower failure rate, pain at the stem tip has been reported by patients with a stemmed tibial component with hybrid fixation [41-43]. Clinical findings indicate that the implant material, as well as stem geometry, are among the major causes of excessive interface micromotion of the stem [44]. Recent efforts to reduce the risk of end-of stem pain have included attempts to improve the tibial component by modifying its macrogeometry and proposals to use

advanced materials such as composites and functionally graded materials [45-47]. The use of advanced materials has reportedly led to enhanced performance in tibiofemoral articulation [48, 49] and bone-implant interface [50]. In a clinical study, Barrack et al. [43] attempted to assess the effect of modifying the implant macrogeometry and material properties on the severity and location of tibial end-of-stem pain following TKA. At a 2 year follow-up, 32% of the patients with a CoCr solid stem experienced end-of-stem pain, whereas only 9.8% of the patients with a slotted titanium stem experienced end-of-stem pain. In a more recent study, Completo et al. [44] postulated that fine-tuning the material properties of the tibial stem tip to make it mechanically similar to that of the surrounding cortical bone could reduce the incidence of post-operative pain. They found that a polyethylene tip lowered the strain at the distal end of the tibial stem, which could contribute to a reduction in the occurrence of end-of-stem pain. Despite these modest improvements in trying to eliminate end-of-stem pain in the proximal tibia, there has been no modification of the tibial implant that has successfully dealt with the modulus mismatch and micromotion that occurs between the stem and the surrounding tibial bone.

The modulus of elasticity mismatch between the tibial component and the host bone results in periprosthetic bone loss in both primary and revision TKA [51]. Recent theoretical advances have made it increasingly clear that the use of implants that are stiffer than the surrounding bone tissue causes bone resorption around the implant [52-55]. The stiffness of bone tissue varies in the range of 4 to 30 GPa depending on the type of bone and the direction of measurement. The value of Young's modulus for chromium alloys and titanium alloys are 220 and 110 GPa, respectively – much higher than that of bone tissue. This significant discrepancy between the elastic modulus of bone and implant results in a large portion of the loads being transferred to the implant, and thus causing bone to be under-loaded. The biological characteristics of bone enable it to adjust to the mechanical and physiological loads by adding tissue at locations undergoing high stress and removing it from under-loaded parts [25]. As a result, the understimulated parts of bone begin to lose mass through an adaptive process known as bone resorption. Bone resorption around a knee implant can lead to a subsequent periprosthetic fracture and decrease the amount and quality of bone at the time of revision surgery. On the other hand, adjusting the tibial implant stiffness to values in the order of magnitude of the surrounding cancellous bone has proven effective for reducing bone resorption in the proximal tibia [56]. However, due to the homogeneous distribution of elastic properties in

the stem, the amount of stress shielding around the tip of the stem remains considerable. Tawkol [57] found that customizing the elastic modulus within the tibial tray could contribute to a 46% reduction in the stresses transferred to the implant, thus resulting in less bone resorption. This reduction can be achieved by varying the elastic modulus from 40 GPa at the top of the tray to 110 GPa downward. Other strategies that deal with the resolution of the modulus mismatch between standard titanium implants and the surrounding tibia involve the use of highly porous materials, such as tantalum foam [58]. Although its biocompatibility and high volumetric porosity can provide an exceptional degree of compliance, tantalum foam has a quasi-uniform distribution of pores. Consequently, it has limited capacity to minimize bone resorption and interface micromotion simultaneously. On the other hand, when the porous architecture is graded with properties that are mechanically biocompatible with those of the native bone tissue, the results are encouraging. This strategy has recently been adopted in the design of a hip replacement implant that can facilitate osseointegration and concurrently minimize bone resorption and bone-implant interface failure [52-55]. While this work focused on the suppression of bone resorption in a hip implant, the same strategy can be extended to deal with stress shielding and micromotion that occur in present-day stemmed tibial implants used in TKA.

## 1.4 Thesis Objective

The objective of this thesis is to introduce a fully porous cementless stemmed tibial knee implant for primary and revision knee replacement surgeries. The proposed implant features a 3D cellular microarchitecture tailored to concomitantly minimize interface micromotion and bone resorption, while satisfying clinical strength and fatigue requirements. To design the 3D microstructure of the implant, we propose a systematic methodology integrating multiscale mechanics and topology optimization to optimally customize the distribution of mechanical properties within the lattice microstructure of the implant. The methodology aims at designing a flexible open-cell lattice for the microstructure of the implant such that the distribution of mechanical properties of the implant mimics that of the surrounding bone tissue and thus minimizes post-operative complications, namely bone resorption and interface micromotion.

The major problem associated with the fully solid tibial implants currently on the market is the post-operative pain which mainly occurs around the tip of the stem of the implant. As previously described, the end-of-stem pain results from excessive interface micromotion at the bone-implant interface. The main cause of interface micromotion can be attributed to the mismatch between the material properties of the implant and those of the bone tissue which causes the latter to be underloaded and therefore leads to preprosthesis bone resorption. The incidence of bone resorption results in lower mechanical support at the bone-implant interface; hence micromotion occurs at the bone-implant interface as a result of a weak mechanical support.

It is hypothesized in this thesis that a tailored lattice microarchitecture of the implant can address both bone resorption and interface micromotion problems associated with the current fully solid implants. The optimally designed porous microstructure of the tibial implant can improve the load-bearing capacity of the implant, thus resulting in a more even load distribution between the implant and the surrounding bone tissue. The proposed cellular tibial implant features mechanical properties similar to those of the tibia and is capable of alleviating the postoperative pain. Additionally, the fatigue resistance of the implant is ensured by including in the optimization problem the minimum allowable fatigue safety factor of the implant determined by the relevant ASTM standards.

## 1.5 Thesis Organization

In Chapter 2, the process of creating the finite element (FE) model of the tibia and the implant as well as assigning the inhomogeneous properties of the bone is described. This chapter discusses the computational method of asymptotic homogenization, which is used to characterize the mechanical properties of the tetrahedron lattice unit cell used as the building block of the implant microarchitecture. It also details the calculations of the fatigue surface of the tetrahedron lattice, as well as the fatigue theory used to capture the safety factor of the implant.

Chapter 3 describes the theory of topology optimization and discusses the advantages and limitations of the optimization scheme proposed in this thesis. In addition, the governing equations used to describe the compliance of the tibial knee microarchitecture are presented. A sensitivity analysis of the objective function and the density filter function utilized to avoid a checker-board pattern for the implant microstructure is also detailed.

Chapter 4 applies the proposed methodology to the design of the first fully porous tibial knee implant. The performance of the proposed tibial knee implant, in particular its interface micromotion and bone resorption, is then assessed and compared to that of two baseline concepts. The first is a fully solid one that is commercially available, and the second is a fully porous tibial implant identical to the fully solid one, but with uniform distribution of pores. Finally, conclusions and suggestions for future work are presented in chapter 5.

## Chapter 2: Theory and Methods

### 2.1 Introduction

This chapter introduces a methodology based on multiscale mechanics and topology optimization to synthesize a graded cellular tibial knee implant that can concurrently minimize bone resorption and interface micromotion. A solid model of the tibial knee implant and tibia are created and used to capture the mechanics of the implant at both macro and micro scales. An asymptotic homogenization (AH) technique is utilized to obtain the macro stress distribution within the implant and bone. The major mathematical formulation of the AH theory is described and applied to characterize the mechanical properties of the tetrahedron unit cell.

### 2.2 Methodology

Elastic property tailoring for hip stems was introduced in the 1990s as a promising mean to reduce bone resorption [59, 60]. Whereas those studies focused on the use of functionally graded solid materials, only recently porous materials with tailored cellular architecture have been successfully exploited to locally tailor the implant compliance so as to reduce bone resorption, and to customize material porosity for enhanced bone ingrowth and implant stability [52-55, 61]. In this work, we present a fully porous biomaterial for a tibial knee implant, specifically a stemmed tibial component, with tailored properties and macro geometry identical to that of a commercially available tibial component, as explained in detail in the following section [62-67]. Figure 15 briefly depicts the strategy proposed here. The mechanical properties of the building block are expressed as a function of its relative density, and their optimal gradients are determined via topology optimization starting from the tissue properties of the tibial native bone of a patient.

The major aspects of the proposed methodology rest on the integration of multiscale mechanics and hierarchical optimal design of materials [68, 69], as briefly summarized in the steps below:

- CT scan data from a 38 year old male are used to create the finite element (FE) model of his tibial geometry and bone tissue properties.
- An open cell, a Tetrahedron-based topology, is selected to modularly build the interior architecture of the porous tibial stem. The high strength characteristics of

this unit cell ensure a minimum level of fatigue and static resistance, as deemed necessary to resist the set of repetitive loads the knee is subjected to [61]. Asymptotic homogenization is used to calculate the elastic constants of the unit cell stiffness tensor, with characteristic length much smaller than the implant, as a function of its relative density [65, 70-73].

- A first trial uniform distribution of relative density is assigned to the implant and 3D finite element analysis is undertaken. From this analysis, the stress and displacement regime over the prosthesis geometry is obtained and used to formulate a multi constraint topology optimization problem. On the microscale, the stress distribution over the lattice architecture is retrieved and used to determine the implant safety factor (SF) under static and fatigue conditions.
- To minimize bone resorption and interface micromotion around the tibial stem, topology optimization is solved for maximum implant compliance. The problem is also subjected to a set of inequality and equality constraints, which include average porosity of the cellular implant, along with safety factors for first cycle and infinite fatigue life. Implant compliance is obtained from the calculation of the total strain energy of the implant. Implant displacements at each mesh element node along with unit cell homogenized properties are then used to build the macro stiffness tensor of each element. The gradient of the objective function is then obtained through partially taking the gradient of the stiffness tensor with respect to its relative density.
- The design variables are grouped in the vector,  $\mathbf{b}$ , which collects the relative density of all elements and is updated via an optimality criterion. The optimization process continues until the attainment of the optimised distribution of relative density.



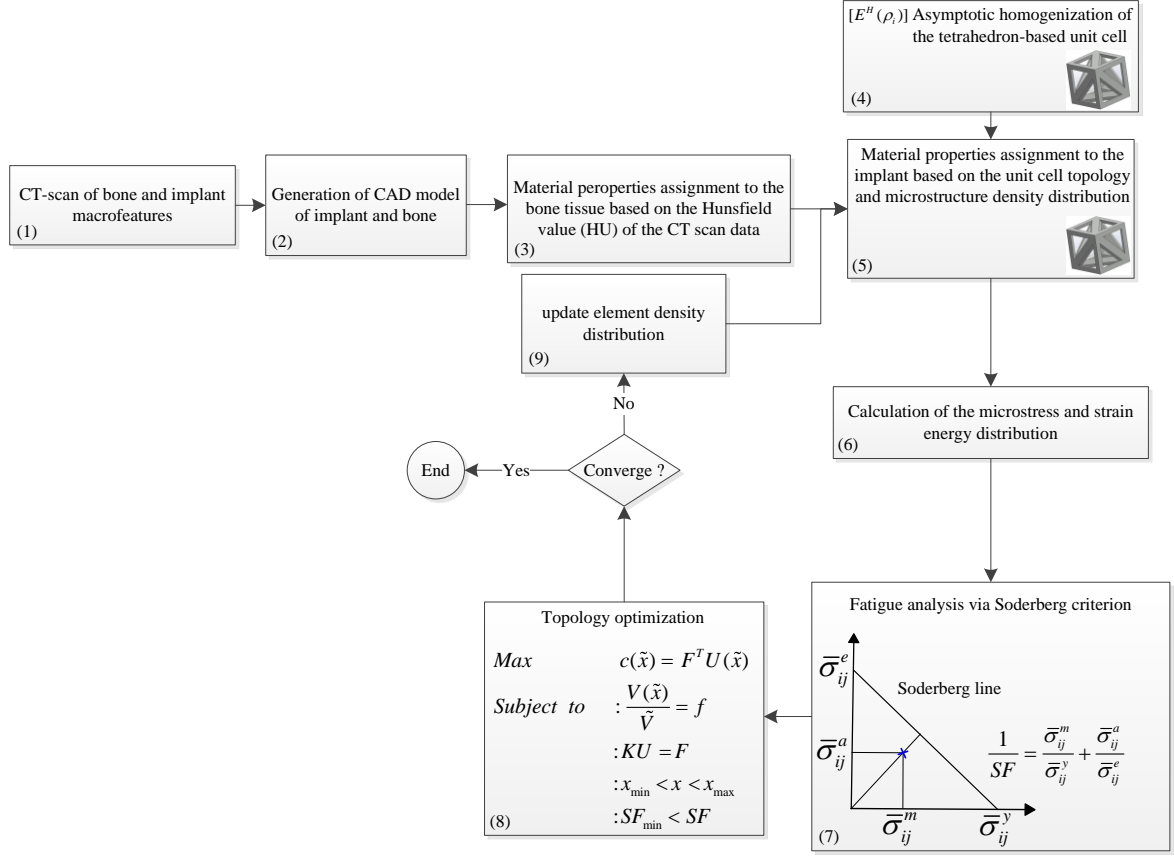
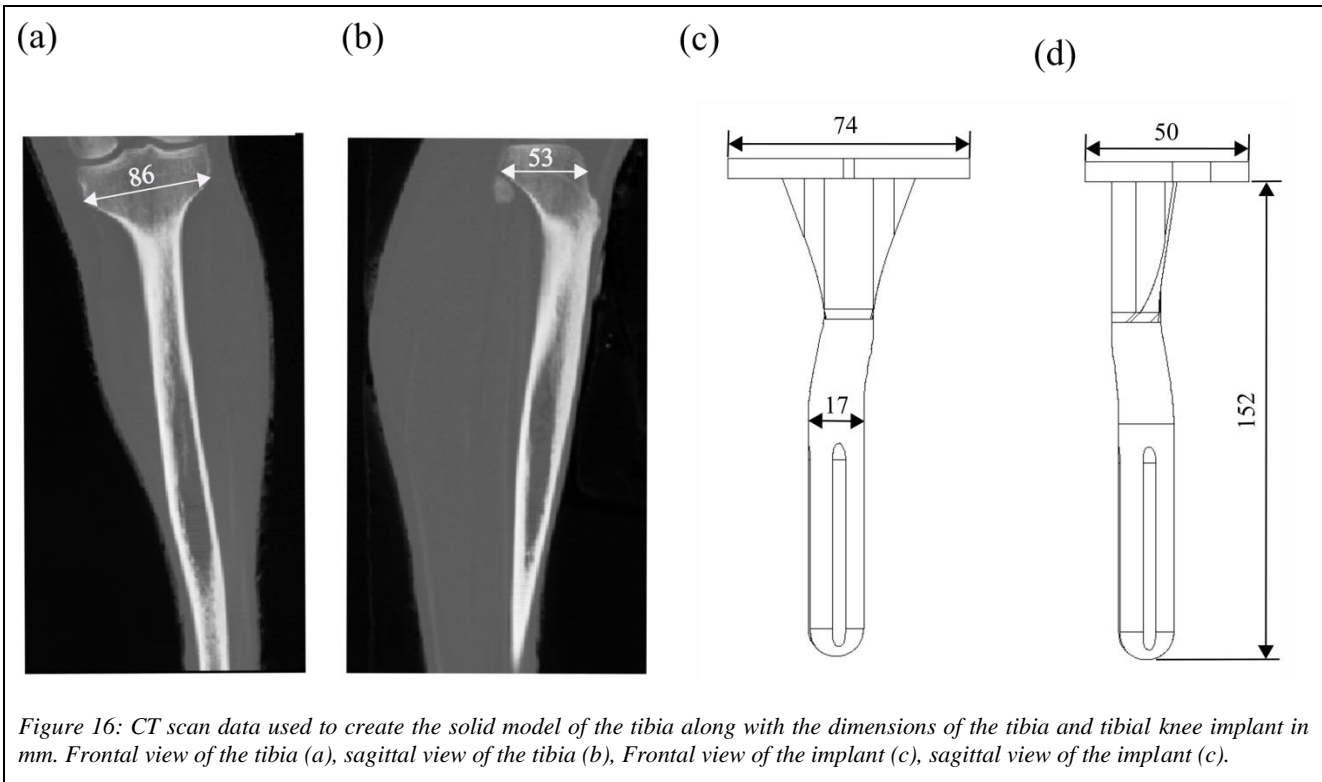


Figure 15; Flow chart illustrating the analysis and design scheme used to develop a graded cellular knee implant minimizing bone resorption and interface micromotion.

## 2.3 Finite Element Model

The three-dimensional (3D) finite element (FE) model of the tibial fixation is constructed through CT images from the left tibiae of a 38 year old male with a body weight of 900 N, as shown in Figure 16. The properties of bone are assumed to be isotropic, a simplification that does not lead to a considerable difference from the results that consider bone as orthotropic [74, 75]. The effective Young's modulus of each element is obtained through the apparent density of the corresponding element. The Hounsfield values (HU) obtained through the CT images are used to determine the apparent density of bone by using a linear interpolation between HU and apparent density. As a result, the effective elastic properties of bone are expressed as a function of the apparent density [74, 76, 77]. The procedure followed to compute the mechanical properties of the tibia is detailed in **Appendix A**.



The macrogeometry of the stemmed tibial knee implant was taken from a NexGen component (Zimmer, Warsaw, IN) commercially available and made of solid titanium. The tibial dimensions were measured and the tibia was templated using NexGen templates to determine the appropriate size of the tibial component and the tibial stem. The component was sized to ensure the central portion of the tibial tray was externally rotated to lie over the medial 1/3 of the tibial tubercle while choosing the largest size possible that would cover the proximal tibia, 10 mm below the articular surface, but did not overhang. The tibial stem was chosen to fill the proximal tibial diaphysis. An offset tibial stem was required to permit anatomic positioning of the tibial tray and ensure centralization of the stem. This resulted in using a size 5 NexGen stemmed tibial implant with a 4 mm offset 100 mm stem extension, creating in a 145 mm offset stem. These implants were CT scanned to create the parameters used in this study. The identical macrogeometry was then used to convert the solid stemmed tibial implant into the optimized 3D porous implant here proposed.

Figure 17 shows the geometry of the intact and implanted bone along with the applied loads and boundary conditions. The distal end of the bone is fixed to avoid rigid body motion. As clinically recommended, the exterior of the implant stem is made of a thin shell that eases the

implant removal during revision surgery. This ensures that in a postoperative situation no bone ingrowth occurs onto the stem, which is press fitted into the cortical bone. On the other hand, the implant tray is kept fully porous, and for this reason bone ingrowth can occur beneath it. To accurately capture interface stability, two distinct contact models are implemented in this work, one for the tray and one for the stem below. The tibial tray is assumed fully bonded to the underlying bone of the tibial plateau; this scenario represents the incidence of bone ingrowth onto the tray. One benefit of this choice is the reduction in the computational cost required for the stability analysis on a non-linear frictional contact model [78]. On the other hand, a frictionless contact is assumed for the tibial stem below the tray, where a thin solid shell covers the implant. This contact model represents the weak bonding between the smooth metal and the surrounding bone tissue [78, 79]. At the bone implant interface, face to face contact elements with appropriate mesh type are used with results that show interfacial micromotion at an average error of about 10 $\mu$ m [78]. The entire stem surface is selected as the target member and the inner bone surface is selected to be the contact member. The Augmented Lagrangian method, where contact penetration is present but controlled to some degree, is used in the contact formulation and contact tractions are monitored at the Gauss points. A contact stiffness of 1 is considered at the contact regions. The time step control is set to be automatic, where the contact behaviour is reviewed at the end of each substep to ensure that neither drastic change in contact status nor excessive penetration occurs.

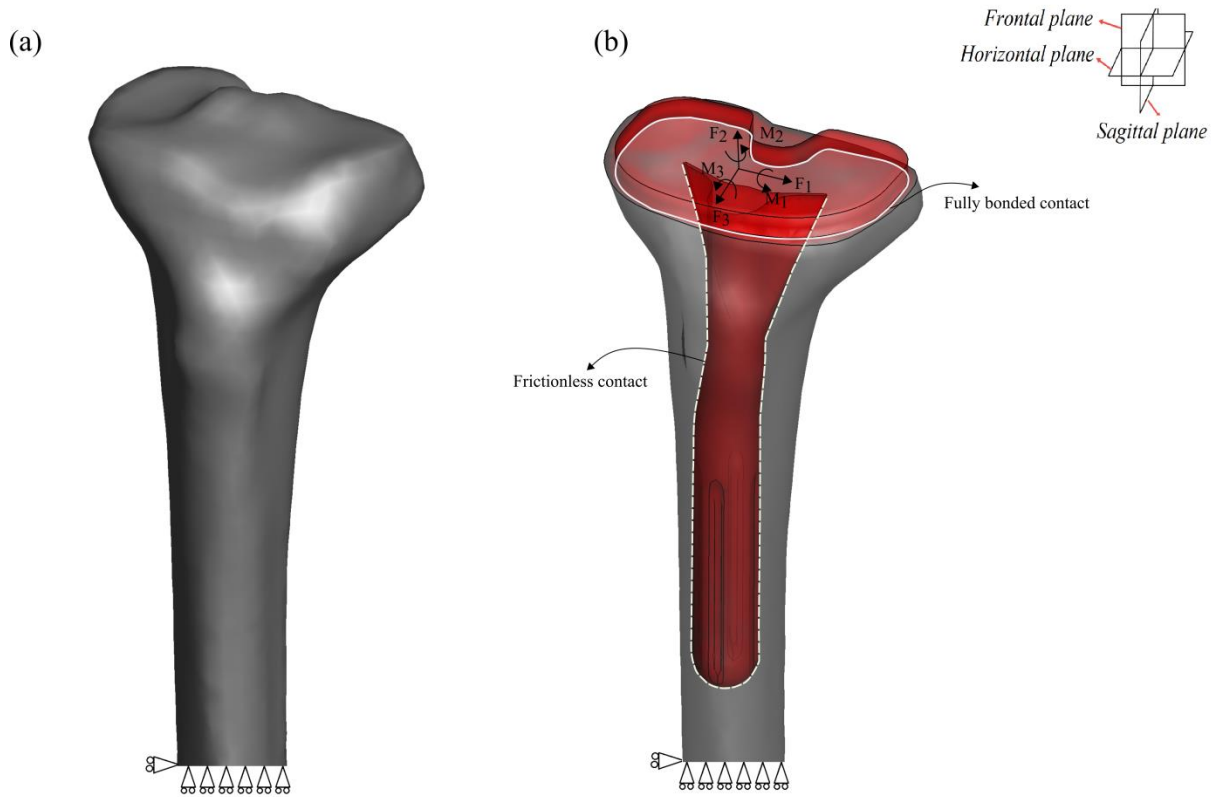


Figure 17: 3D finite element model of the intact tibiae (a), and implanted prosthesis (b).

Four different load cases corresponding to the 20%, 30% and 40% of the gait cycle and deep-knee bend are all studied. The system of loads reported in Table 1 and adopted in this work represents the daily physiological loads experienced by a human. Obtained from in-vivo measurements on an instrumented knee joint, those values pertain to a subject with a male body weight of 1000N and provide contact load measures with an error below 2% [80-82]. The values in Table 1 are used with equal weights to calculate an equivalent load pattern that represents concurrently walking and deep knee bend, and is here used for the implant design.

Table 1: Loading conditions used in this study.  $F_1$ ,  $F_2$  and  $F_3$  act in the medio-lateral, vertical and posterior-anterior directions respectively.  $M_1$ ,  $M_2$  and  $M_3$  act in the sagittal, horizontal and frontal plane of the tibiae, as shown at the right top corner in Fig 17.

	No.	Load case	Force / N			Moment / N.mm		
			$F_1$	$F_2$	$F_3$	$M_1$	$M_2$	$M_3$
Level walking	1	20% of gait cycle	-76.05	-318.9	-169.96	2420	-1900	3430
	2	30% of gait cycle	-144.65	-1442.14	52.79	3760	1090	-4790
	3	40% of gait cycle	-71.96	-2141.34	61.18	8850	1070	20220
Level bending	4	Deep knee bend	75.8	-2537.57	-8.3	13220	-2230	12030

## 2.4 Homogenized Mechanical properties

Mechanics and optimization of implant microarchitecture are here undertaken by treating the implant as a homogenized continuum, an assumption that allows to avoid detailed finite element simulations, which would be extensive and lengthy to handle [83]. By doing so, we can focus on a representative volume element (RVE) of the implant, and consider its properties as those of a homogenized medium equivalent to the implant itself. Below is a description of the method used in this thesis to calculate the stiffness tensor and implant fatigue resistance, which both depend on multiscale properties, specified at the macro and micro scale.

### 2.4.1 Homogenization Techniques

Cellular materials are hybrid materials made of voids and interconnected network of solid struts or plates. Inspired by natural materials with cellular microstructure, artificial cellular materials have been recently engineered. They offer a large range of mechanical properties where some of them are not covered by traditional fully bulk materials. They are also broadly utilized in industrial applications where weight saving or multifunctional properties are critical. Aerospace sandwich panels, vibration and sound insulators, compact heat exchangers, and biomedical implants are a few examples [29, 84-86]. Cellular materials are generally divided into two main categories: stochastic and ordered, depending on the arrangement of the cells. Most natural cellular materials are stochastic as their cells generally are randomly arranged. Lattice materials, on the other hand, feature a one, two or three dimensional periodic arrangement of cells [25].

The characteristic length of the component in cellular materials is larger than that of its constituent building block, e.g. unit cell size. To analyze these materials using a direct approach

requires modeling every single strut of the entire lattice microstructure. Despite the accuracy of this approach, the associated computational cost would result in considerably large models which are often impractical to manage [25].

Various techniques proposing analytical, numerical and experimental methods to capture the mechanical properties of lattices exist in the literature. They have their own limitations and advantages that make them suitable to be used dependent on the problem and model. Recent noteworthy efforts to understand the behaviour of cellular material provide closed-form expressions of their effective properties [85, 87-89]. In these studies, the assumption of Euler-Bernulli beam for the struts has been taken into consideration and the effective properties of the struts have been derived through solving equilibrium and deformation problems. For simple cell topologies shown in Figure 18, macroscopic stresses have been applied and the deformation as well as stress distribution throughout the cell walls have been determined to calculate the in-plane elastic stiffness and strength of the material [89, 90].

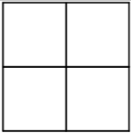


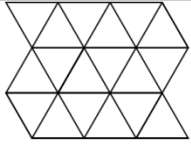
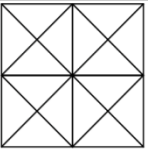
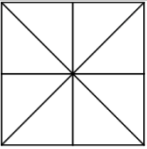
Bending dominated		Stretching dominated			
					
Square	Hexagonal	Kagome	Triangular	Mixed triangular A	Mixed triangular B

Figure 18: Common cell topologies used to generate lattice structures [25].

Although this approach is reasonably accurate to predict the properties of cellular materials, it has limitations in the case of complex cell topologies. Other methods including matrix-based techniques have been recently utilized to homogenize the properties of planar lattices. These methods benefit from Bloch's theorem and the Cauchy-Born hypothesis to formulate the microscopic nodal deformations of a lattice in terms of its macroscopic strain field from which the macroscopic elastic tensor is derived [91].

Recently, an asymptotic homogenization (AH) approach that replaces a cellular structure with a representative volume featuring identical mechanical properties has been successfully exploited to model and analyze lattice materials with periodic arrangement of cells [65, 71, 72, 92]. This approach has already been used for the analysis of composite materials and topology

optimization of structures [62, 66, 93, 94]. AH assumes an asymptotic expansion for any field quantity and then uses it to derive the governing equations of equilibrium and predicting the effective properties. The accuracy and reliability of AH have been proved through several experimental studies [95-98]. In an experimental work by Takano et al. [97], a comparison between the deformed microstructure of knitted fabric composite materials obtained through respectively AH method and experiment was performed and a good agreement between the results was observed. In another study, the predicted elastic modulus of a porous alumina with a porosity of 3.1% using AH was within 1% of that determined through experiments. This result proves the high reliability of AH [98]. Another underlying advantage of AH is that the stress distribution within the unit cell can be determined and used to perform a detailed analysis of strength and damage of the material [92, 99, 100]. AH can furthermore be used to handle any type of lattices regardless of relative density or complexity of the unit cell.

The selection of the homogenization technique is critical to the accuracy of the results as well as the computational cost required to determine the effective properties. This presents a trade-off that should be considered while selecting the homogenization method. For instance, the theoretical hypothesis that offers closed-form expressions can be conveniently used to rapidly compute the effective properties. However, in case of large values of relative densities and complex cell units, this approach shows limitations. On the other hand, methods that provide accurate results over the whole range of relative densities are generally associated with a longer time of computation [100].

## 2.4.2 Elastic properties of unit cell

To obtain the homogenized properties of the knee implant examined in this work, we use AH theory. The yield and ultimate strength of lattice materials are assessed for relative density  $\rho < 0.3$  and used to obtain the implant stiffness tensor and capture the fatigue strength of the designed implant via the Soderberg fatigue criterion under multi axial stresses [101].

The effective properties of the building block  $E_{ijkl}^H$  are obtained by solving a local problem formulated on the RVE and defined as [102]:

$$E_{ijkl}^H = \frac{1}{|Y|} \int_{Y_C} E_{ijpm} M_{pmkl} dY \quad (1)$$

Where  $|Y|$  is the unit cell volume,  $E_{ijpm}$  is the positional elastic tensor of the unit cell that varies between zero and the material elastic tensor corresponding to the voids and bulk material respectively. Furthermore, we define a structure tensor  $M_{pml d}$  that relates the local macro strains  $\bar{\epsilon}_{kl}$  to the micro strains as

$$\epsilon_{ij} = M_{ijkl} \bar{\epsilon}_{kl} \quad (2a)$$

$$M_{ijkl} = \frac{1}{2}(\delta_{ik}\delta_{jl} + \delta_{il}\delta_{jk}) - \epsilon_{ij}^{*kl} \quad (2b)$$

Where  $\delta_{ij}$  is the Kronecker  $\delta$ , and  $\epsilon_{ij}^{*kl}$  is the microscopic strain corresponding to the component  $kl$  of the macroscopic strain. Given that for this application small deformation and linear elasticity hold, the microscopic strain  $\epsilon_{ij}^{*kl}$  can be expressed as

$$\int_{Y_C} E_{ijpm} \epsilon_{ij}^1(v) \epsilon_{pm}^{*kl}(u) dY = \int_{Y_C} E_{ijkl} \epsilon_{ij}^1(v) \bar{\epsilon}_{kl} dY \quad (3)$$

where  $\epsilon_{ij}^1(v)$  denotes the virtual strain.

For a three-dimensional case, six arbitrary macroscopic unit strains are required to construct the  $M_{ijkl}$  matrix. The periodicity of the strain field is ensured by imposing periodic boundary conditions on the RVE edges [102, 103]. As a result, the nodes of the opposite planes are set with identical displacement. Once the structure tensor,  $M_{ijkl}$ , is obtained, the homogenized stiffness tensor of the unit cell can be predicted by substituting the structure tensor  $M_{pmkd}$  into (1). The microscopic stress distribution,  $\sigma_{ij}$ , can be defined by

$$\sigma_{ij} = E_{ijkl} M_{klmn} \bar{\epsilon}_{mn} \quad (4)$$

Using the microscopic stress tensor and introducing the homogenized elastic tensor,  $E_{rs mn}^H$ , results in a simplified relationship between the microscopic stress distribution and the macroscopic stress tensor

$$\sigma_{ij} = E_{ijkl} M_{klmn} (E_{rs mn}^H)^{-1} \bar{\sigma}_{rs} \quad (5)$$

wherein  $\bar{\sigma}_{rs}$  is the macroscopic stress distribution applied to the RVE. If  $\sigma_{ys}$  is the yield strength of the cell walls, then the yield surface of the unit cell can be written from (5) as



$$\bar{\sigma}_{ij}^y = \frac{\sigma_{ys}}{\max\{\sigma_{vm}(\bar{\sigma}_{ij})\}} \bar{\sigma}_{ij} \quad (6)$$

Where  $\sigma_{vm}(\bar{\sigma}_{ij})$  is the von-Mises stress distribution within the unit cell caused by the applied macroscopic stress  $\bar{\sigma}_{ij}$ .

Figure 19 illustrates the predicted elastic moduli and yield strength of the unit cell used in this work for the tibial knee-implant, obtained for the generic case of multi axial loadings. A relative density ranging  $0.01 < \rho < 1$  can be considered for the unit cell; however, since the cell topology degenerates for  $\rho > 0.8$ , we consider values of  $\rho$  between 0.05 and 0.8 only.

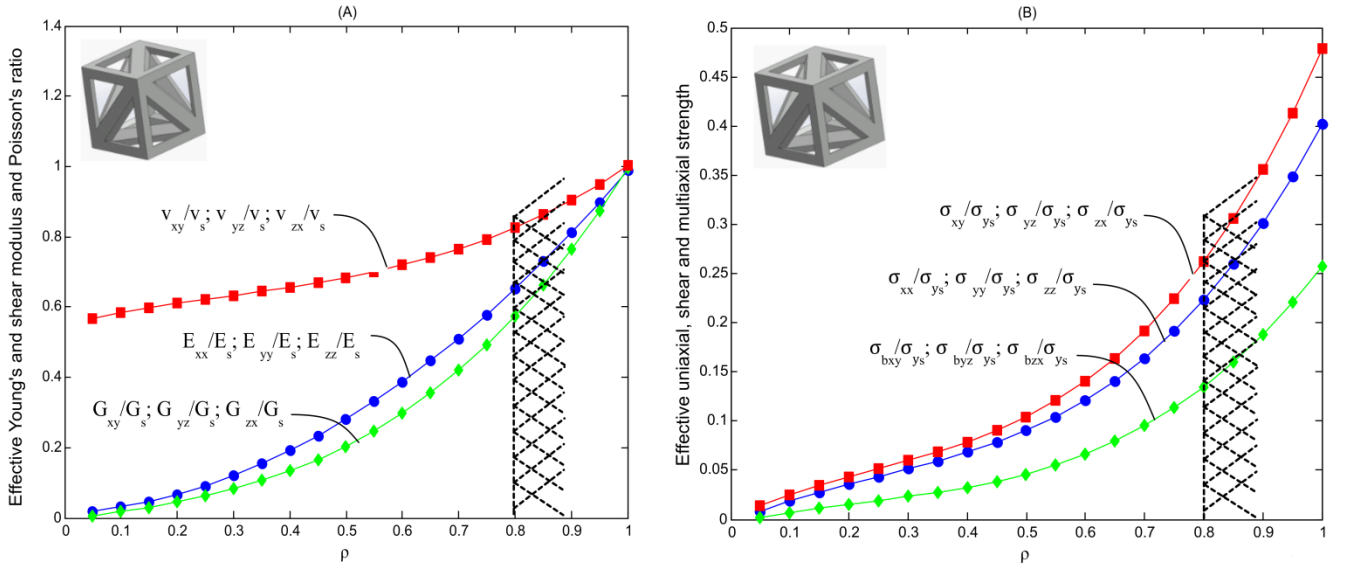


Figure 19: (A) Effective elastic and (B) effective strength properties of Tetrahedron based lattice as a function of relative density. Effective elastic properties and yield strengths normalized with respect to elastic properties and yield strengths of bulk material. Only three independent elastic constants are necessary for the tetrahedron-based cell which is orthotropic and has 3 planes of symmetry: (Young's modulus),  $G_{xy}$  (Shear modulus) and  $\nu_{yz}$  (Poisson's ratio).  $\sigma_{xx}$ ,  $\sigma_{xy}$  and  $\sigma_{bxy}$  refer to uniaxial, shear and biaxial strength respectively. Values of  $\rho$  above 0.8 are dismissed due to cell topology degeneration.

### 2.4.3 Fatigue properties

Implant stiffness tailoring is undertaken against high cycle fatigue failure such that stress values generated within the material architecture do not exceed Ti6Al4V yield strength, the material the implant is made of. Hence, to obtain the fatigue surface  $\bar{\sigma}_{ij}^e$  of the RVE, we multiply the RVE yield strength  $\bar{\sigma}_{ij}^y$  by the ratio of the endurance limit  $\sigma_{es}$  and yield strength  $\sigma_{ys}$  of the solid material. This gives

$$\bar{\sigma}_{ij}^e = \bar{\sigma}_{ij}^y \frac{\sigma_{es}}{\sigma_{ys}} \quad (7)$$

Once the fatigue surface is obtained, the Soderberg diagram, a conservative criterion, can be constructed to compute the fatigue safety factor,  $SF_{fatigue}$ , from the relation:

$$\frac{\bar{\sigma}_{ij}^m}{\bar{\sigma}_{ij}^y} + \frac{\bar{\sigma}_{ij}^a}{\bar{\sigma}_{ij}^e} = \frac{1}{SF_{Fatigue}} \quad (8)$$

wherein,  $\bar{\sigma}_{ij}^m$  and  $\bar{\sigma}_{ij}^a$  denote the mean and alternating stresses respectively, given by:

$$\bar{\sigma}_{ij}^m = \frac{\bar{\sigma}_{ij}^{\max} + \bar{\sigma}_{ij}^{\min}}{2} \quad (9a)$$

$$\bar{\sigma}_{ij}^e = \frac{\bar{\sigma}_{ij}^{\max} - \bar{\sigma}_{ij}^{\min}}{2} \quad (9b)$$

With  $\bar{\sigma}_{ij}^{\max}$  and  $\bar{\sigma}_{ij}^{\min}$  being the multi-axial macroscopic stresses that cause, respectively, the highest and the lowest von-Mises stress within the unit cell. From eq. (5) and (6), the static safety factor of the RVE is expressed as:

$$SF_{static} = \frac{\bar{\sigma}_{ij}^y}{\sigma_{ij}} \quad (10)$$

The procedure above is used for the analysis of the tibia knee implant which is modelled with homogenized properties representing the tetrahedron-based cell made of Ti6Al4V [104]. The properties of Ti6Al4V here adopted (Young's modulus: 120 GPa, Poisson's ratio: 0.3, yield strength: 900 MPa, fatigue strength: 600 MPa at 10<sup>7</sup> cycles) are measured from mechanical testing of 3d-printed samples manufactured via Selective Laser Melting [105]. SLM is the additive process that will be used for implant fabrication. In this work, we rely on the assumption that defects and imperfections emerging from the manufacturing process would not severely impact the mechanical properties [55, 61]. Further work, currently undergoing, is required to include the influence of manufacturing deviations in the implant analysis [106].

## 2.5 Conclusion

The first part of this chapter has presented a systematic methodology for the design of a graded cellular knee implant. The methodology is developed and followed to engineer a new

fully porous tibial knee implant. A solid model of the tibia and the implant have been created through the CT data obtained from a patient. The second part has discussed the basic concept as well as the computational formulation of AH method used in this thesis to design the implant. The AH theory has then been applied to characterize the mechanical properties of the tetrahedron based cell unit. The effective elastic modulus and yield stress of the tetrahedron unit cell have been obtained for the whole range of relative density.

Lastly, a numerical method based on the Soderberg fatigue diagram has been presented to design the lattice microstructure of the implant against fatigue failure. The method has been used to capture the fatigue safety factor of the implant throughout the optimization process.

The formulation of the topology optimization procedure utilized to find the optimum material distribution throughout the implant appears in the next chapter. The optimization process is integrated with the multiscale mechanics scheme described in this chapter so as to obtain the derivative of the objective function with respect to the design variable, i.e. the relative density of the lattice.

## Chapter 3: Topology Optimization algorithm

Based on the multiscale mechanics theory described in Chapter 2 as well as the fundamental gradient-based topology optimization algorithm reported in the literature, an optimization scheme is proposed in this chapter to find the optimum gradients of material distribution. AH theory, described in Chapter 2, is integrated with the optimization procedure to ease the calculations of the gradients of the objective function. The main goal of this chapter is to provide the formulation of the optimization problem and the derivative of the objective function with respect to the design variables. In Chapter 4, the optimization scheme is applied to the design of a fully porous tibial knee implant.

### 3.1 Classical topology optimization

A structural optimization problem can be categorized as a shape, sizing or topology optimization as depicted in Figure 20. An example of sizing optimization is to address the distribution of thickness over a plate with the goal of minimizing or maximizing a certain physical quantity and subject to equilibrium and other constraints on the state. For sizing optimization, the design domain and state variables are known and fixed whereas the goal of shape optimization is to find the optimum shape of a predefined domain. Hence, in shape optimization, the boundaries of the domain are the design variables. During shape optimization, the topology never goes through any changes, such that no holes will be added or removed from the domain [107].

Topology optimization is a computational strategy used to characterize the material distribution within a specified domain without a preconceived shape. This underlying feature provides topology optimization with an exceptional capability of designing innovative, high-performance structural layouts, which can meet several constraints simultaneously. A topology optimization problem can be defined as a binary problem which aims to find a black and white layout within a prescribed domain that minimizes the work done by external forces. A general problem of shape optimization formulated as finding the optimum material distribution is a starting point for topology optimization [108].

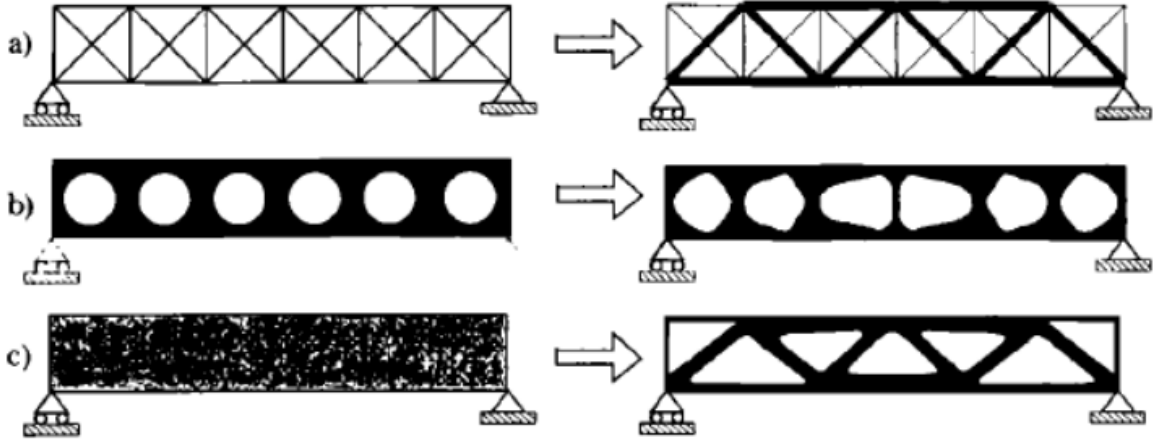


Figure 20: The initial (left) and final (right) designs of sizing (a), shape (b) and topology optimization (c) [107].

The problem of finding the optimum material distribution in topology optimization is equivalent to determining the optimum elastic stiffness tensor for a specified solid body which is variable over the domain. A typical approach to determine the optimum topology is to discretize the domain into finite elements [109]. To avoid the difficulties of auto meshing in case of generating random holes, a fixed mesh is used where low values of stiffness properties is assigned to the void elements representing holes [67]. In addition, the displacement and stiffness fields are meshed through the prescribed mesh. Hence, the minimization problem can be formulated as [109]:

$$\begin{aligned}
 & \text{Min} \quad f^T u \\
 & \text{subject to} \quad K(E_e)u = f \\
 & \quad \quad \quad E_e \in E_{ad}
 \end{aligned} \tag{11}$$

where  $f$  and  $u$  are the load and displacement vectors respectively, the stiffness matrix  $K$  is a function of  $E_e$  in an element  $e$ , and  $E_{ad}$  is the set of admissible stiffness tensors for the given problem [109]. The stiffness matrix  $K$  can be defined as the sum of the stiffness of each element:

$$K = \sum_{e=1}^N K_e(E_e) \tag{12}$$

where the element  $e$  is numbered as  $e = 1, \dots, N$  and  $K_e$  is the global element stiffness matrix.

The classical binary compliance problem is known to be a non-convergent approach which gradually reduces the compliance of the structure [110-112]. A recent alternative procedure that

avoids a binary layout is referred to the density-based approach which relaxes the binary condition and incorporates the intermediate material densities in the problem formulation. In a density-based method, the mechanical properties of the structure, namely stiffness properties are related to the density distribution through a penalization approach which implicitly penalizes elements with intermediate density values. This penalization procedure is usually referred to the solid isotropic material with penalization (SIMP) method [113]. The penalization method is generally used when a grey region in the final topology, which refers to intermediate densities, is not desired.

### 3.2 Optimization methods

In the literature, there are numerous studies focusing on the compliance problem. These efforts aim at introducing new approaches with high ability to improve the manufacturability of the final topology [114-117]. The current approaches commonly used in the literature for topology optimization include optimality criteria (OC) method, the method of moving asymptotes (MMA), and the level set method (LSM) [118]. The two most common gradient based methods that are compatible with topology optimization are described below.

#### 3.2.1 Optimality criteria method

The optimality criteria (OC) method is a simple updating scheme used to update the design variables in topology optimization. It is a heuristic method based on the Lagrangian function for which the update of each design variable is independent from the other design variables [119].

The Lagrangian function for the optimization problem can be defined by

$$L = c + \lambda(V - fV_0) + \lambda_1^T(Ku - f) + \sum_{e=1}^N \lambda_{2e}(x_{\min} - x_e) + \sum_{e=1}^N \lambda_{3e}(x_e - x_{\min}) \quad (13)$$

wherein  $\lambda$  and  $\lambda_1$  are the global Lagrangian multipliers and  $\lambda_{2e}$  and  $\lambda_{3e}$  are the Lagrangian multipliers for lower and upper side constraints.

Optimum results are found by setting the derivative of the Lagrangian function with respect to the design variables to zero which takes the particular form as:

$$\frac{\partial L}{\partial x_e} = 0, \text{ for } e=1, N \quad (14)$$

$$\frac{\partial L}{\partial x_e} = \frac{\partial c}{\partial x_e} + \lambda \frac{\partial V}{\partial x_e} + \lambda_1^T \frac{\partial ku}{\partial x_e} - \lambda_{2e} + \lambda_{3e}$$

The derivative of the Lagrangian functions can be simplified as the lower and upper bound constraints can be assumed inactive and the applied loads independent from the design variables [119]. Hence, the derivative of the Lagrangian function becomes:

$$\frac{\partial L}{\partial x_e} = u^T \frac{\partial K}{\partial x_e} u + \lambda_1^T \frac{\partial K}{\partial x_e} u + \frac{\partial u}{\partial x_e} (2u^T K + \lambda_1^T K) + \lambda v_e \quad (15)$$

The term  $\frac{\partial u}{\partial x_e}$  can be eliminated by assigning a proper value to  $\lambda_1^T$  and the derivative of the Lagrangian function may be expressed as:

$$\frac{\partial L}{\partial x_e} = -p(x_e)^{p-1} u_e^T K_0 u_e + \lambda v_e = 0 \quad (16)$$

where  $u_e^T K_0 u_e$  denotes the strain energy of a solid element with density 1. Since the strain density remains constant throughout the design domain, the design variables can be updated based on

$$\frac{p(x_e)^{p-1} u_e^T K_0 u_e}{\lambda v_e} = \frac{\partial x_e}{\lambda v_e} = B_e^k = 1 \quad (17)$$

The heuristic scheme to update the design variables can then be obtained using (17) and may be expressed as:

$$x_e^{k+1} = x_e^k \left( \frac{p(x_e)^{p-1} u_e^T K_0 u_e}{\lambda v_e} \right)^\xi = x_e^k (B_e^k)^\xi \quad (18)$$

wherin  $\xi$  is a damping coefficient varying between zero and one. To stabilize the process of updating the design variables so that a smooth change in the density of a certain element between two successive iterations is ensured, a positive move limit  $m$  is introduced. This move limit does not allow big change in relative density between two successive iterations so that an element does not go from void to solid in one iteration. Hence, the heuristic OC scheme for updating the design variables takes the form

$$x_e^{k+1} = \begin{cases} \max(x_{\min}, x_e^k - m) & \text{if } x_e^k (B_e^k)^\vee \leq \max(x_{\min}, x_e^k - m) \\ x_e^k (B_e^k)^\vee & \text{if } \max(x_{\min}, x_e^k - m) < x_e^k (B_e^k)^\vee < \min(x_{\min}, x_e^k + m) \\ \min(1, x_e^k + m) & \text{if } x_e^k (B_e^k)^\vee \geq \min(1, x_e^k + m) \end{cases} \quad (19)$$

The OC algorithm described above has been widely used in a large number of structural topology problems. Although it is well known to be effective and quick for large scale problems, it suffers from several limitations including mesh dependence, checkerboard patterns and computational inefficiency, factors that limit its functionality. Checkerboard patterns problem occur when void and solid elements are connected by corners only, thus resulting in high stiffness regions. This approach is also not suitable for multi objective optimization problems with multi constraints because OC can be used with one objective function only [119].

### 3.2.2 Method of Moving Asymptotes

The method of moving asymptotes (MMA) is a general and flexible updating scheme based on a special type of convex approximation. This approach is capable of handling smooth, nonlinear optimization problems as well as various types of design variables including element size, shape variables and material orientation angle. It is known to be a stable updating approach which generates a sequence of improved feasible solutions of the optimization problem [120].

MMA creates a sequence of simpler approximation subproblems to solve the optimization problem. The subproblems are convex and separable, which are derived based on the sensitivity of a given design point and the previous iterations. The major features of MMA can be summarized as follows [120]:

- It is an explicit rational, strictly convex function for all values of the design variables,  $x$  such that  $L_j^{(k)} < x_j < U_j^{(K)}$  where  $L_j^{(k)}$  and  $U_j^{(K)}$  are the lower and upper bound asymptotes at each iteration. In addition, the function is monotonic such that it increases for  $\frac{\partial f}{\partial x_j}(x^{(k)}) > 0$  and decreases when  $\frac{\partial f}{\partial x_j}(x^{(k)}) < 0$ .
- It is smooth so that the approximation functions  $\tilde{f}^{(k)}$ , are continuous and twice differentiable over the interval of  $L_j^{(k)} < x_j < U_j^{(K)}$ .
- At each iteration, a sequence of subproblems that are simpler approximation, is generated and solved using the current point  $x^{(k)}$ . The solutions of the



subproblems determine the next iteration  $x^{(k+1)}$  so that only a single inner iteration is performed.

However, since MMA is based on a first order approximation, it does not provide any information about the curvature of the approximation function resulting in convergence problems. Improving the MMA approach remains a challenge in the literature. Recently, an intense amount of work has attempted to address the problem of convergence by introducing a diagonal second derivative of the objective function for which the curvature of the approximation function can be captured through selecting ideal parameters in MMA [121].

### 3.3 Numerical problems in topology optimization

As described in the previous section, topology optimization algorithms are usually associated with several numerical problems, such as mesh-dependency, checkerboard pattern and local minima [63]. Mesh dependency, illustrated in Figure 21, is a numerical instability which results in a larger number of holes in the final topology as the mesh refinement increase. Ideally, an increased mesh refinement is expected to improve the modeling of the boundaries, however, topology optimization is associated with a non-existence of numerical solutions due to the problem of mesh independency.

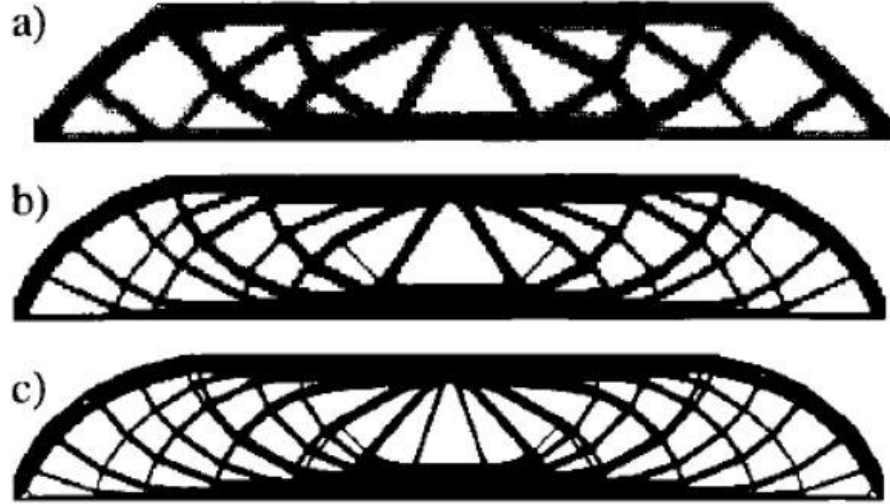
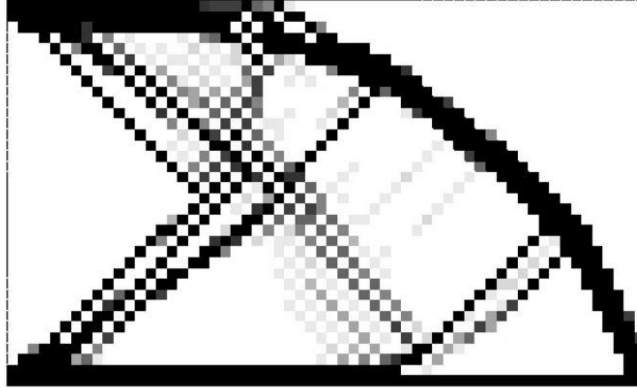


Figure 21: Optimum topology obtained for a mesh of (a) 2700, (b) 2800 and (c) 17200 elements. As the number of elements increase and mesh refines, the issue of mesh dependency leads to more holes in the optimum topology [63].

Ending up with a topology featuring a checkerboard pattern, as shown in Figure 22, is another underlying problem associated with topology optimization. Checkerboard patterns result

in jagged boundaries as well as solid elements surrounded by void elements. Such a topology, on one hand leads to stress concentration specifically around the boundaries and on the other hand has a low manufacturability [122].



*Figure 22: A cantilever beam featuring a poor optimum topology as a result of checkerboard pattern topology [122].*

To overcome such numerical problems, numerous regularization techniques have been offered so as to alleviate the problem of layouts with high degree of discontinuity by introducing some filtering opportunities [123]. One highly effective filter to address the problem of mesh dependency is to modify the design sensitivities such that the sensitivity of each element is dependent on the sensitivities of neighboring elements within a fixed range. This is a heuristic method of filtering which has been proved to be computationally efficient and simple to implement. In addition, higher order mesh elements and local gradient constraints can be used to improve the manufacturability of the final topology.

Other filtering techniques include the restriction of the possibility of the optimum solutions by adding extra constraints namely density variation filters, on the design space of the admissible design vectors. This goal can be achieved by including filters in the optimization problem or reducing the parameter space directly. This ensures the convergence of the finite element approximation [107].

### **3.4 Optimization Scheme**

In this thesis, a density-based topology optimization is adopted to optimally tailor the material distribution in the stem of the tibial component [124]. The search for the optimized density gradients is undertaken on an equivalent medium with homogenized properties obtained

in section 2.4.2 and expressed as a function of relative density (Figure 19). A penalization scheme that penalizes elements with intermediate density values is used to create an implant with continuous density distribution [113].

### 3.4.1 Problem formulation

Elastic stiffness tailoring aims at reducing the elastic modulus mismatch between implant microstructure and native bone, resulting in lower bone resorption. As such, to minimize bone-stem interface micromotion and bone resorption, the optimization problem is posed for minimum stiffness, which is equivalent to maximize implant compliance [125], here expressed as

$$c(\tilde{x}) = F^T U(\tilde{x}) \quad (20)$$

where  $F$  is the vector of the nodal forces applied to the implant and  $U(\tilde{x})$  is the vector of nodal displacement.  $F$  can be expressed as

$$F = K(\tilde{x}) U(\tilde{x}) \quad (21)$$

where  $K(\tilde{x})$  is the total stiffness matrix of the implant [126]. The problem is subjected to multiple constraints, e.g. on volume, density, and safety factor, and can be formally formulated as:

$$\begin{aligned} \text{Find} \quad & x = [x_1, x_2, \dots, x_e, \dots, x_n] \\ \text{Maximize} \quad & c(\tilde{x}) = F^T U(\tilde{x}) \\ \text{subject to} \quad & v(\tilde{x}) = \tilde{x}^T v - \tilde{v} \leq 0 \\ & x \in \chi \quad \chi = \{x \in R^n : x_{\min} \leq x \leq x_{\max}\} \\ & SF_{\min} < SF \end{aligned} \quad (22)$$

where  $\tilde{x}$  is the density vector which is filtered through a basic filter function described in **Appendix B**,  $n$  is the total number of the elements that discretizes the implant domain,  $V=[v_1, \dots, v_n]$  is the vector of the elements volume and  $\tilde{v}$  is a prescribed volume of the tibial knee implant.

The optimization problem defined in (23) can be reformulated as a traditional problem of minimization by multiplying the objective function by -1, which results in

$$\begin{aligned}
&\text{Find} && x = [x_1, x_2, \dots, x_e, \dots, x_n] \\
&\text{Minimize} && c(\tilde{x}) = -F^T U(\tilde{x}) \\
&\text{subject to} && v(\tilde{x}) = \tilde{x}^T v - \tilde{v} \leq 0 \\
&&& x \in \mathcal{X} \quad \mathcal{X} = \{x \in R^n : x_{\min} \leq x \leq x_{\max}\} \\
&&& SF_{\min} < SF
\end{aligned} \tag{23}$$

The derivative of the objective function can be determined as:

$$\frac{\partial c(\tilde{x})}{\partial x_e} = \sum_{i \in N_e} \frac{\partial c(\tilde{x})}{\partial \tilde{x}_i} \frac{\partial \tilde{x}_i}{\partial x_e} \tag{24}$$

where  $\tilde{x}_i$  represent the filtered density of element  $i$  and  $\frac{\partial \tilde{x}_i}{\partial x_e}$  is defined by

$$\frac{\partial \tilde{x}_i}{\partial x_e} = \frac{H_{ie} v_e}{\sum_{j \in N_i} H_{ij} v_j} \tag{25}$$

where  $H_{ij}$  is a weight factor matrix as described in **Appendix B**. From (24),  $\frac{\partial c(\tilde{x})}{\partial \tilde{x}_i}$  can be defined by

$$\frac{\partial c(\tilde{x})}{\partial \tilde{x}_i} = -F^T \frac{\partial U(\tilde{x})}{\partial \tilde{x}_i} = -U^T(\tilde{x}) K(\tilde{x}) \frac{\partial U(\tilde{x})}{\partial \tilde{x}_i} \tag{26}$$

where  $F^T$  and  $U^T(\tilde{x})$  indicate the transpose matrix of  $F$  and  $U(\tilde{x})$  respectively. A derivation of (21) with respect to  $\tilde{x}_i$  yields

$$\frac{\partial K(\tilde{x})}{\partial \tilde{x}_i} U(\tilde{x}) + K(\tilde{x}) \frac{\partial U(\tilde{x})}{\partial \tilde{x}_i} = 0 \tag{27}$$

As a result,  $\frac{\partial U(\tilde{x})}{\partial \tilde{x}_i}$  can be expressed as follows:

$$\frac{\partial U(\tilde{x})}{\partial \tilde{x}_i} = -K(\tilde{x})^{-1} \frac{\partial K(\tilde{x})}{\partial \tilde{x}_i} U(\tilde{x}) \tag{28}$$

From (26) and (28), we can obtain the derivative of the objective function as

$$\frac{\partial c(\tilde{x})}{\partial \tilde{x}_i} = U(\tilde{x})^T \frac{\partial K(\tilde{x})}{\partial \tilde{x}_i} U(\tilde{x}) \tag{29}$$

The procedure followed to calculate the derivative of the stiffness matrix of the implant microstructure with respect to the design variables appears in the following section. Once the sensitivity of the objective function is obtained, the design variables are updated using the optimality criterion (OC) scheme [115] until convergence is reached, as described in **Appendix C**.

### 3.4.2 Derivation of the stiffness tensor for the implant internal microstructure

To compute the sensitivity of the strain energy of the implant microstructure, as described in section 3.4.1, the derivative of the stiffness tensor is required for the entire implant microstructure. We use here a direct stiffness approach to find the global stiffness tensor, where the implant is discretized into small elements and the elastic tensor of each element is calculated before the global stiffness matrix,  $K$ , assembly, where  $K$  is expressed as

$$K = \int_{\Omega} B_i^T D_i B_i dV \quad (30)$$

$B$  is the strain-displacement matrix and  $D$  is the elastic tensor of element  $i$ , and  $\Omega$  is the total volume of the implant. Since the strain-displacement matrix is independent of the design variables, the derivation of the stiffness matrix with respect to the design variables (relative density of each element) can be expressed as follows:

$$\frac{\partial K}{\partial x_i} = \int_{\Omega} B_i^T \frac{\partial D_i}{\partial x_i} B_i dV \quad (31)$$

Each mesh element corresponds to a Tetrahedron-based cell that has three planes of symmetry; therefore 9 elastic constants are needed in the constitutive equations: 3 Young's moduli  $E_x, E_y, E_z$ , 3 Poisson's ratios  $\nu_{yz}, \nu_{zx}, \nu_{xy}$  and 3 shear moduli  $G_{yz}, G_{xy}, G_{xz}$ . The stiffness matrix of the unit cell can thus be expressed as

$$D = \begin{bmatrix} \frac{1 - \nu_{yz} \nu_{zy}}{E_y E_z \Delta} & \frac{\nu_{yx} + \nu_{zx} \nu_{yz}}{E_y E_z \Delta} & \frac{\nu_{zx} + \nu_{yx} \nu_{zy}}{E_y E_z \Delta} & 0 & 0 & 0 \\ \frac{\nu_{xy} + \nu_{xz} \nu_{zy}}{E_z E_x \Delta} & \frac{1 - \nu_{zx} \nu_{xz}}{E_z E_x \Delta} & \frac{\nu_{zy} - \nu_{zx} \nu_{xy}}{E_z E_x \Delta} & 0 & 0 & 0 \\ \frac{\nu_{xz} + \nu_{xy} \nu_{yz}}{E_x E_y \Delta} & \frac{\nu_{yz} + \nu_{xz} \nu_{yx}}{E_x E_y \Delta} & \frac{1 - \nu_{xy} \nu_{yx}}{E_x E_y \Delta} & 0 & 0 & 0 \\ 0 & 0 & 0 & 2G_{yz} & 0 & 0 \\ 0 & 0 & 0 & 0 & 2G_{zx} & 0 \\ 0 & 0 & 0 & 0 & 0 & 2G_{yx} \end{bmatrix} \quad (32)$$

$$\Delta = \frac{1 - \nu_{xy} \nu_{yx} - \nu_{yz} \nu_{zy} - \nu_{zx} \nu_{xz} - 2\nu_{yz} \nu_{zx} \nu_{xy}}{E_x E_y E_z}$$

Since AH is used to obtain the elastic constants of the unit cell across a range of relative densities, with results shown in Figure 19, we can represent the elastic tensor of each element as a function of the element relative density and then use it to evaluate the derivative of the elastic tensor with respect to the design variables. The strain-displacement matrix is also derived by differentiating the displacements expressed through shape functions and nodal displacements. A 10 nodes isoparametric Tetrahedron element is used to mesh the FE model of implanted tibia. Hence, the strain-displacement matrix can be written as

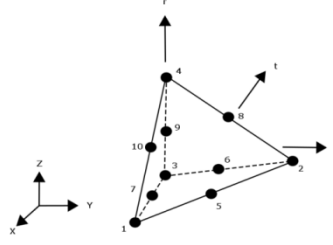
$$B = [B_1 \ B_2 \ B_3 \ B_4 \ B_5 \ B_6 \ B_7 \ B_8 \ B_9 \ B_{10}] \quad (33)$$

With

$$B_k = \begin{bmatrix} N_{k,x} & 0 & 0 \\ 0 & N_{k,y} & 0 \\ 0 & 0 & N_{k,z} \\ N_{k,y} & N_{k,x} & 0 \\ 0 & N_{k,z} & N_{k,y} \\ N_{k,z} & 0 & N_{k,x} \end{bmatrix} \quad k \in (1, 2, \dots, 10) \quad (34)$$

Where  $N_{k,x}$ ,  $N_{k,y}$  and  $N_{k,z}$  are the derivative of the shape functions with respect to the global coordinate system. The shape functions of a Tetrahedron element with respect to the isoparametric natural coordinate system given by r, s and t can be defined as

$$\begin{aligned}
N_1 &= 2s^2 - s \\
N_2 &= 2t^2 - t \\
N_3 &= 2r^2 - r \\
N_4 &= 2r^2 + 4rs + 4rt - 3r + 2s^2 + 4st - 3s + 2t^2 - 3t + 1 \\
N_5 &= 4st \\
N_6 &= 4rt \\
N_7 &= 4rs \\
N_8 &= 4s - 4rs - 4st - 4s^2 \\
N_9 &= 4t - 4rt - 4st - 4t^2 \\
N_{10} &= 4r - 4rs - 4rt - 4r^2
\end{aligned} \tag{35}$$



To construct the strain-displacement matrix, the derivative of the shape functions with respect to the generalized coordinate system is computed via the chain rule as

$$\frac{\partial N}{\partial r} = \frac{\partial N}{\partial x} \frac{\partial x}{\partial r} + \frac{\partial N}{\partial y} \frac{\partial y}{\partial r} + \frac{\partial N}{\partial z} \frac{\partial z}{\partial r} \tag{36a}$$

$$\frac{\partial N}{\partial s} = \frac{\partial N}{\partial x} \frac{\partial x}{\partial s} + \frac{\partial N}{\partial y} \frac{\partial y}{\partial s} + \frac{\partial N}{\partial z} \frac{\partial z}{\partial s} \tag{36b}$$

$$\frac{\partial N}{\partial t} = \frac{\partial N}{\partial x} \frac{\partial x}{\partial t} + \frac{\partial N}{\partial y} \frac{\partial y}{\partial t} + \frac{\partial N}{\partial z} \frac{\partial z}{\partial t} \tag{36c}$$

Using the (36), results in

$$\begin{bmatrix} \frac{\partial N_k}{\partial x} \\ \frac{\partial N_k}{\partial y} \\ \frac{\partial N_k}{\partial z} \end{bmatrix} = \begin{bmatrix} \frac{\partial x}{\partial r} & \frac{\partial y}{\partial r} & \frac{\partial z}{\partial r} \\ \frac{\partial x}{\partial s} & \frac{\partial y}{\partial s} & \frac{\partial z}{\partial s} \\ \frac{\partial x}{\partial t} & \frac{\partial y}{\partial t} & \frac{\partial z}{\partial t} \end{bmatrix} \begin{bmatrix} \frac{\partial N_k}{\partial r} \\ \frac{\partial N_k}{\partial s} \\ \frac{\partial N_k}{\partial t} \end{bmatrix} = [J] \begin{bmatrix} \frac{\partial N_k}{\partial r} \\ \frac{\partial N_k}{\partial s} \\ \frac{\partial N_k}{\partial t} \end{bmatrix} \tag{37}$$

where  $[J]$  is the Jacobian matrix. From (38), the Jacobian matrix of a 10 nodes Tetrahedron element may be expressed as [126]

$$\begin{bmatrix} \frac{\partial N_1}{\partial r} & \frac{\partial N_2}{\partial r} & \frac{\partial N_3}{\partial r} & \frac{\partial N_4}{\partial r} & \frac{\partial N_5}{\partial r} & \frac{\partial N_6}{\partial r} & \frac{\partial N_7}{\partial r} & \frac{\partial N_8}{\partial r} & \frac{\partial N_9}{\partial r} & \frac{\partial N_{10}}{\partial r} \\ \frac{\partial N_1}{\partial s} & \frac{\partial N_2}{\partial s} & \frac{\partial N_3}{\partial s} & \frac{\partial N_4}{\partial s} & \frac{\partial N_5}{\partial s} & \frac{\partial N_6}{\partial s} & \frac{\partial N_7}{\partial s} & \frac{\partial N_8}{\partial s} & \frac{\partial N_9}{\partial s} & \frac{\partial N_{10}}{\partial s} \\ \frac{\partial N_1}{\partial t} & \frac{\partial N_2}{\partial t} & \frac{\partial N_3}{\partial t} & \frac{\partial N_4}{\partial t} & \frac{\partial N_5}{\partial t} & \frac{\partial N_6}{\partial t} & \frac{\partial N_7}{\partial t} & \frac{\partial N_8}{\partial t} & \frac{\partial N_9}{\partial t} & \frac{\partial N_{10}}{\partial t} \end{bmatrix} \begin{bmatrix} x_1 & y_1 & z_1 \\ x_2 & y_2 & z_2 \\ x_3 & y_3 & z_3 \\ x_4 & y_4 & z_4 \\ x_5 & y_5 & z_5 \\ x_6 & y_6 & z_6 \\ x_7 & y_7 & z_7 \\ x_8 & y_8 & z_8 \\ x_9 & y_9 & z_9 \\ x_{10} & y_{10} & z_{10} \end{bmatrix} \quad (38)$$

where  $\{x_i, y_i, z_i \mid i \in (1, 2, 3, \dots, 10)\}$  are the coordinates of the element nodes. By substituting (37) into (34), the strain-displacement matrix is calculated. Once the strain-displacement matrix for each element is obtained, the gradient of the strain energy for the corresponding element is computed from (31). The sensitivity of the objective function  $\frac{\partial c(\tilde{x})}{\partial \tilde{x}}$  is assembled by the element sensitivity  $\frac{\partial c(\tilde{x})}{\partial \tilde{x}_i}$  to obtain the vector of strain energy differentiation for the whole microarchitecture of the implant. The sensitivity analysis is then implemented under the optimization scheme described in section 3.4.1, to seek the optimum relative density distribution within the implant microstructure.

### 3.5 Conclusion

This chapter has detailed the optimization scheme used to tailor the material distribution of the implant microarchitecture. A gradient based topology optimization has been used to design the lattice microstructure of the implant. Using the AH theory described in Chapter2, the traditional SIMP method has been replaced with the multiscale mechanics to capture the relation of the elastic constants of the implant to its density distribution. The direct stiffness approach is then used to obtain the derivative of the implant compliance in terms of its density distribution. To ensure the convergence of the optimization procedure, the traditional optimality criterion along with a filtering function has been utilized.

The results of the optimization procedure described in this chapter appear in the following chapter. The clinical and mechanical performance of the newly introduced lattice implant are furthermore evaluated and compared to those of the current fully solid implants.



## Chapter 4: Results and Discussion

### 4.1 Introduction

In this chapter, the methodology developed in the previous chapters is applied to the design of a graded cellular tibial knee implant. Two sets of numeric results are presented in this chapter. The first describes the micro-architecture of the proposed tibial implant, and the second its performance, namely bone resorption and bone-stem interface micromotion, which are then compared to those of two baselines, a fully solid titanium tibial implant and a fully porous one with uniform relative density of 60%.

### 4.2 Implant architecture

Figure 23 shows the von Mises distribution and optimal density distribution of the microstructure of the proposed tibial implant which features low porosity at the distal region where severe stresses are located. As can be observed, stress concentration appears beneath the tray due to the variation in implant macrogeometry. In addition, the applied moment in the frontal plane, which represents the Varus-Valgus movement of knee joint, leads to high stress values at the distal region. The tibial implant is fully porous with very low porosity in the tibial tray. In particular, unit cells with high value of relative density ranging 0.7-0.8 are located at regions with high stress in the tibial tray, which ensures a minimum level of fatigue resistance. Hence, underneath the tray as well as in the lower part of the stem, cells with high relative density are necessary to meet the level of fatigue resistance the implant should meet.

From the relative density distribution, the lattice microarchitecture is created through in-house mapping scripts. Figure 23 shows that while the implant internal architecture is fully porous, a very thin shell is placed on the exterior of the stem only. This feature is designed to avoid bone ingrowth onto the stem and thus facilitate the process of implant replacement at the time of revision surgery. While the fully solid tibial implant shows fatigue strength 2 times higher than the cellular tibial implant, the latter has a safety factor of 3.1, which is well within the margin of safety for a biomedical device [127]. If a further increase in the implant fatigue strength is desired, either a lattice with smooth cell geometry could be implemented [101], or other part of the implant could be designed as fully dense.

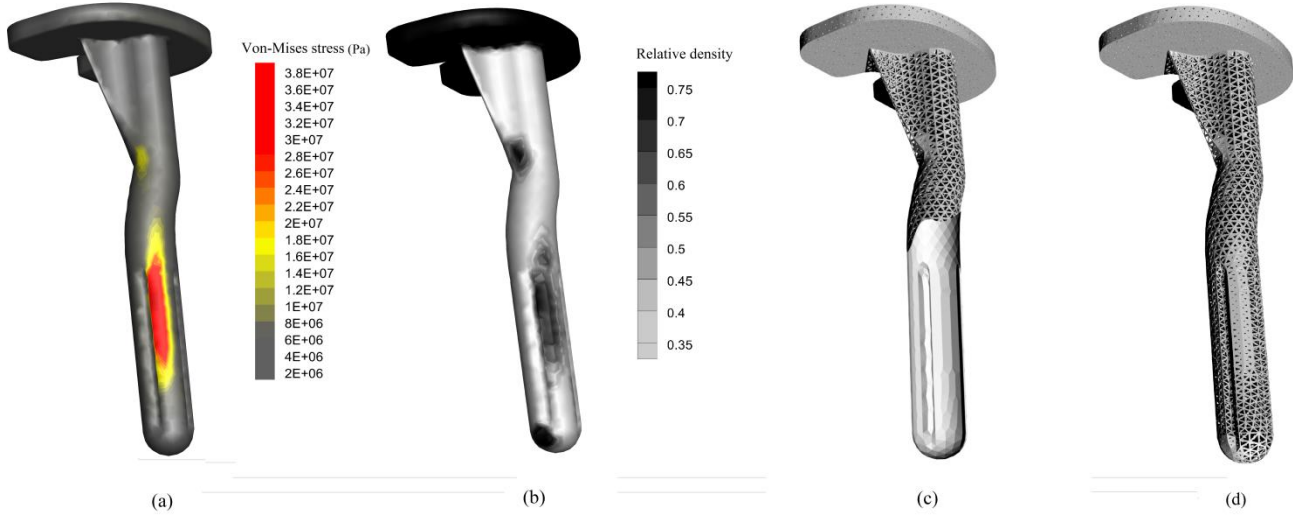


Figure 23: (a) Von-Mises stress distribution; (b) optimum relative density distribution to ensure adequate fatigue resistance against daily cyclic loads; (c) graded cellular implant with tailored porosity in the stem ranging 0.3-0.7. A thin solid exterior (shown only partially in the figure) coats the stem, a clinically recommended feature introduced to ease implant removal at the time of revision surgery; (d) internal architecture of the tibial implant, where the thin shell is here omitted for a global visualization of the whole internal microstructure.

### 4.3 Implant micromotion

The primary stability of the implant is crucial to the success of the total knee arthroplasty (TKA) [128]. An extensive body of the literature has demonstrated that the elastic modulus mismatch from the bone tissue to the implant is one main cause of the lack of stability at the bone-implant interface [38, 44]. Although other factors such as the implant macrogeometry, the fixation technique used at the bone-implant interface, and the design platform of the implant play an important role in the development of interface micromotion [44, 128, 129], in this thesis we address the elastic modulus mismatch. To do so, we perform a relative comparison between implants that share identical macrogeometry and prescribed clinical conditions, such as the fixation type at the bone implant interface. The differences in interfacial micromotion that we observe are therefore relative, and can be exclusively attributed to the distribution of elastic modulus that each tibial implant here examined features.

Figure 24 and 25 illustrate the distribution of bone-stem interface micromotion at 30% of gait cycle and deep bend, respectively. The amount of micromotion is computed from the relative nodal sliding distance of mesh elements from bone and stem. Stable fixation at the bone-stem interface with micromotion between 20 – 50  $\mu\text{m}$  provides a desirable range, since this degree of micromotion is known to be well tolerated by the periprosthetic bone, and in cases of

porous implants, is associated with bone ingrowth [130]. The percentage of surface area (SA) with micromotion below 50  $\mu\text{m}$  is then assessed for the designed graded lattice implant and the two baselines, a fully dense tibial implant and a uniform porosity tibial implant, all made of Ti6Al4V.

Both the loading conditions of gait cycle and deep knee bend led to severe micromotion around the distal part of the stem, particularly around the tip of the stem. High values of micromotion can cause the patient to feel pain at this region. The graded lattice tibial implant stem demonstrated a maximum micromotion at the stem tip that is reduced by 17 $\mu\text{m}$  and 10 $\mu\text{m}$  when compared respectively to a fully solid and a uniform lattice tibial implant stem. This result suggests a lower potential for postoperative end-of-stem pain for patients. As can be seen, the surface area of the graded tibial implant (grey regions of the implant in Figure 24c) is larger than that of the two other implants (Figure 24a and 24b), and induces a micromotion below 50  $\mu\text{m}$ . This value of micromotion ensures an improved stability between the tray periphery and the distal part of the stem. During deep knee bend, a reduction in micromotion of the tip of the stem of 22  $\mu\text{m}$  and 14  $\mu\text{m}$  with respect to a fully dense titanium tibial implant and uniform porosity tibial implant were achieved. This amount represents a 14% reduction in the maximum micromotion at the stem tip for the graded lattice implant compared to the traditional solid implant. This provides the graded tibial implant with 76% prosthesis area with micromotion below 50  $\mu\text{m}$ , values that are clinically stable.

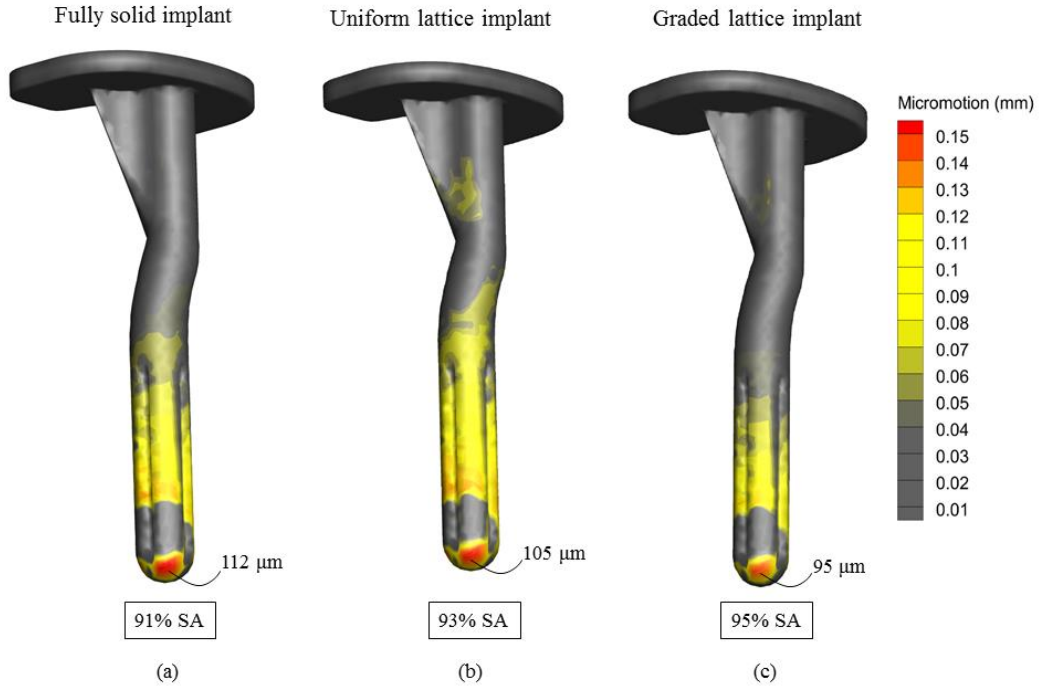


Figure 24: Interface micromotion distribution at 30% of gait cycle for a fully dense titanium implant (a), cellular implant with uniform relative density of 60% (b), and graded cellular implant (c). SA: surface area of the prosthesis.

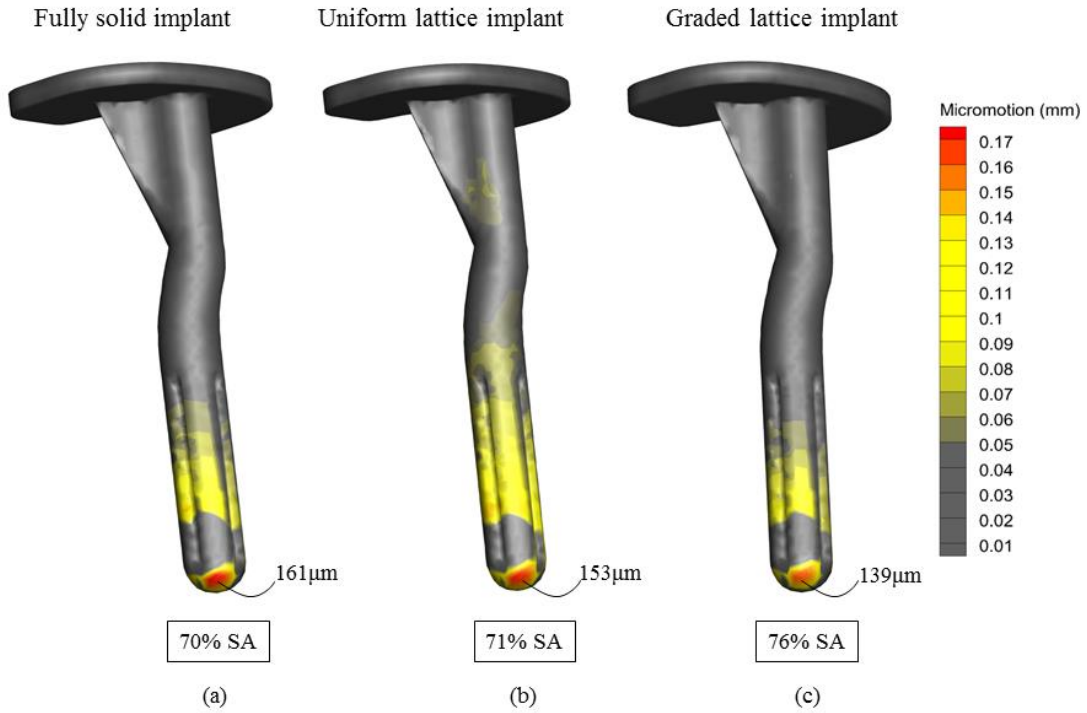


Figure 25: Interface micromotion distribution at deep bend for a fully dense titanium implant (a), cellular implant with uniform relative density of 60% (b), and a graded cellular implant (c). SA: surface area of the prosthesis.

Among the nodal displacement vectors, we now examine the displacement distribution at the mid (i) and distal areas (ii) of the implant, and plot the results in Figure 26. Here, is the micromotion distribution visualized for the loading conditions of walking and deep bend. 50 points around the stem surface have been specified with the first one located at the anterior of the cross section and the remaining ones following a counter clockwise direction. The figure shows sliding micromotion values for deep bend and 30% of gait cycle. As can be seen, the maximum micromotion occurs anteriorly for both loading conditions. The graded lattice implant features a lower value at almost all points around the distal and middle region of the stem, thus resulting in a reduced probability of local interface failure as well as end-of stem pain.

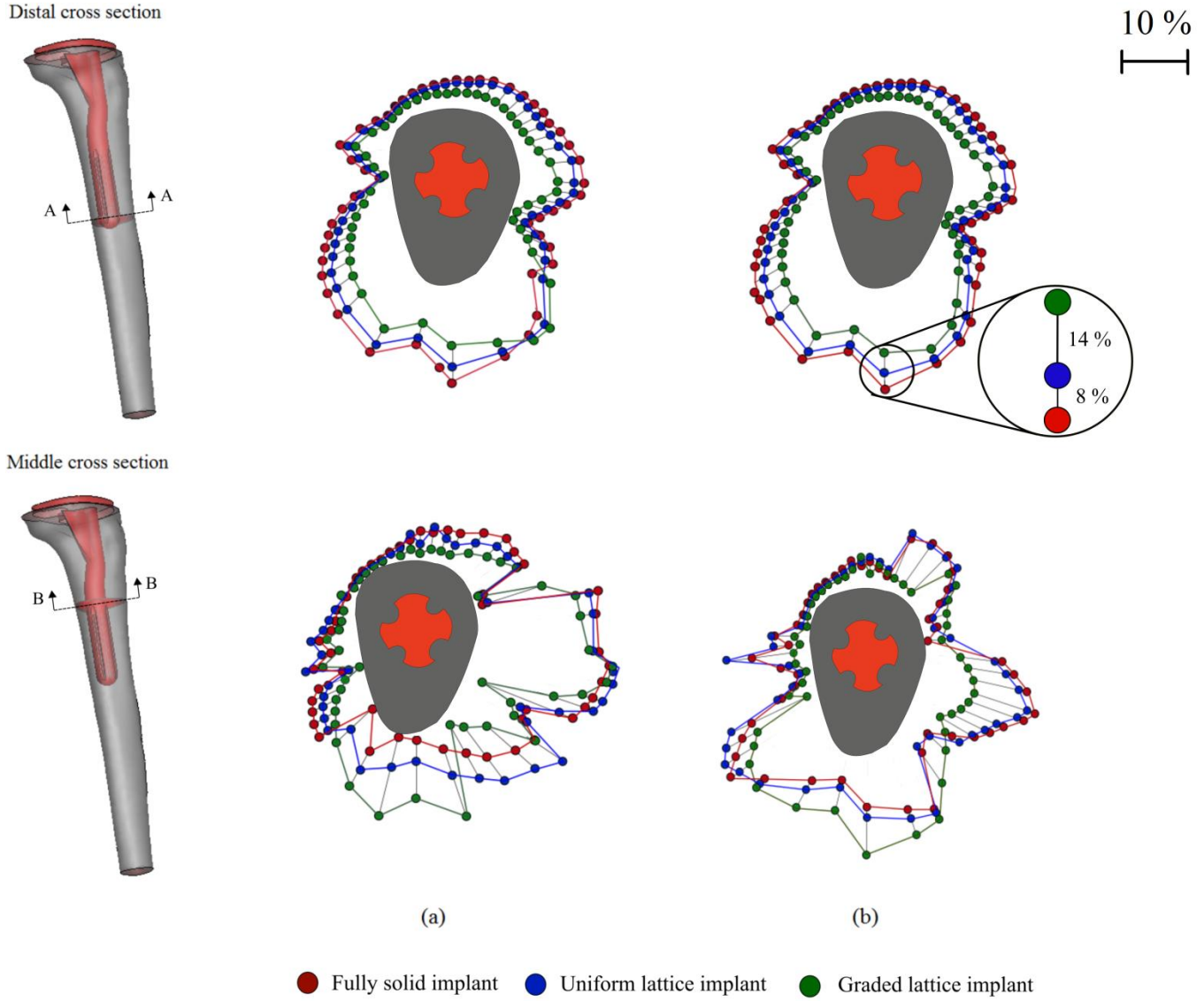


Figure 26: Relative distribution of interface micromotion around the stem surface with respect to the fully solid implant. % values are shown at the distal and mid regions along the stem length for 30% of gait cycle (a), and deep bend (b).

#### 4.4 Bone resorption

To further investigate the improved performance of the implant here introduced, we examine its amount of bone loss compared to that of a fully dense and a uniform porosity tibial implants ( $\rho = 60\%$ ). Figure 27 shows the results with bone resorption levels plotted around the tibial stems in the three cases. The results are obtained by computing the amount of unloaded bone [52-55]. In particular, bone is assumed to start losing its mass when the local strain energy ( $U_i$ ) per unit of bone mass ( $\rho$ ) averaged over ( $n$ ) loading cases ( $S = \left(\frac{1}{n}\right) \sum_{i=1}^n \frac{U_i}{\rho}$ ) in the

postoperative situation is beneath the respective local strain energy of the implant preoperatively  $((1-s) S_{\text{ref}})$ .  $S_{\text{ref}}$  indicates the local strain energy of the intact bone and  $S$  indicates a specialized threshold level or dead-zone for the bone to start degrading after implantation. As a result, the amount of resorbed bone mass can be expressed as

$$m_r(b) = \frac{1}{M} \int_V g(S(b)) \rho dV \quad (39)$$

Where  $M$  and  $V$  are the mass and volume of the original bone and  $g(S(b))$  is a resorptive function equal to unity if  $S < (1-s) S_{\text{ref}}$  and otherwise is equal to zero. The value considered in this study for the dead-zone is 0.75 [59].

We observed that the computed amount of resorbed bone was consistent with the bone-stem stability. The less the bone-stem interface micromotion, the lower bone resorption. As can be seen, significant bone resorption appears proximally underneath the tray throughout the medial compartment of the tibia and propagates toward the lateral part. The concentration of bone resorption in the medial compartment can be attributed to the Varus-Valgus movement of the knee joint which causes a larger portion of the vertical load to be distributed over the medial part of the tibiae.

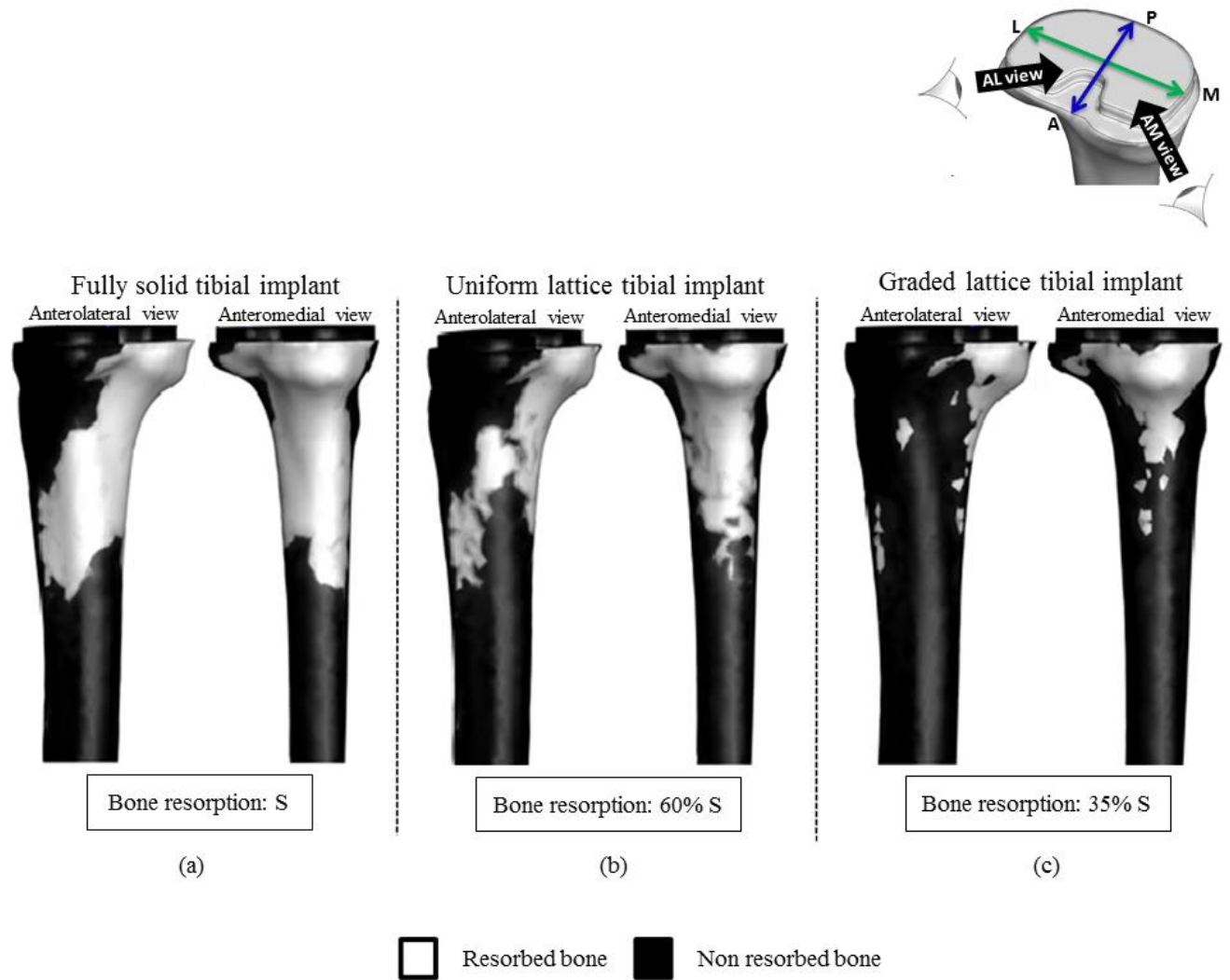


Figure 27: Distribution of bone resorption in knee prosthesis around (a) fully dense titanium implant; (b) cellular implant with uniform relative density of 60%; and (c) graded cellular implant. L: Lateral, M: Medial, A: Anterior, P: Posterior, AL: Anterolateral, AM: Anteromedial.

In Figure 28, we compare the amount of bone resorption at four different regions of the implanted tibia. As previously described, bone resorption is maximum at the proximal region, whereas at the distal regions an overstressed bone results in bone formation [131]. For the solid titanium stem, an overall bone resorption of 40% can be predicted with the greatest degree of resorption occurring in zone 3. Due to the higher compliance of the uniform lattice tibial implant, we observe an overall decrease of resorbed bone of 16%, i.e. two times lower than the solid identical tibial implant. The least amount of bone resorption was seen around the graded cellular implant, with an overall decrease of 26%, 3 times less than that seen around the solid tibial implant. In summary with respect to the fully solid baseline tibial knee implant, Figure 28 shows



a reduction of bone resorption around the graded lattice tibial implant of 50 % at zone 4, 76% at zone 3 54% at zone 2, and 18% at zone 1.

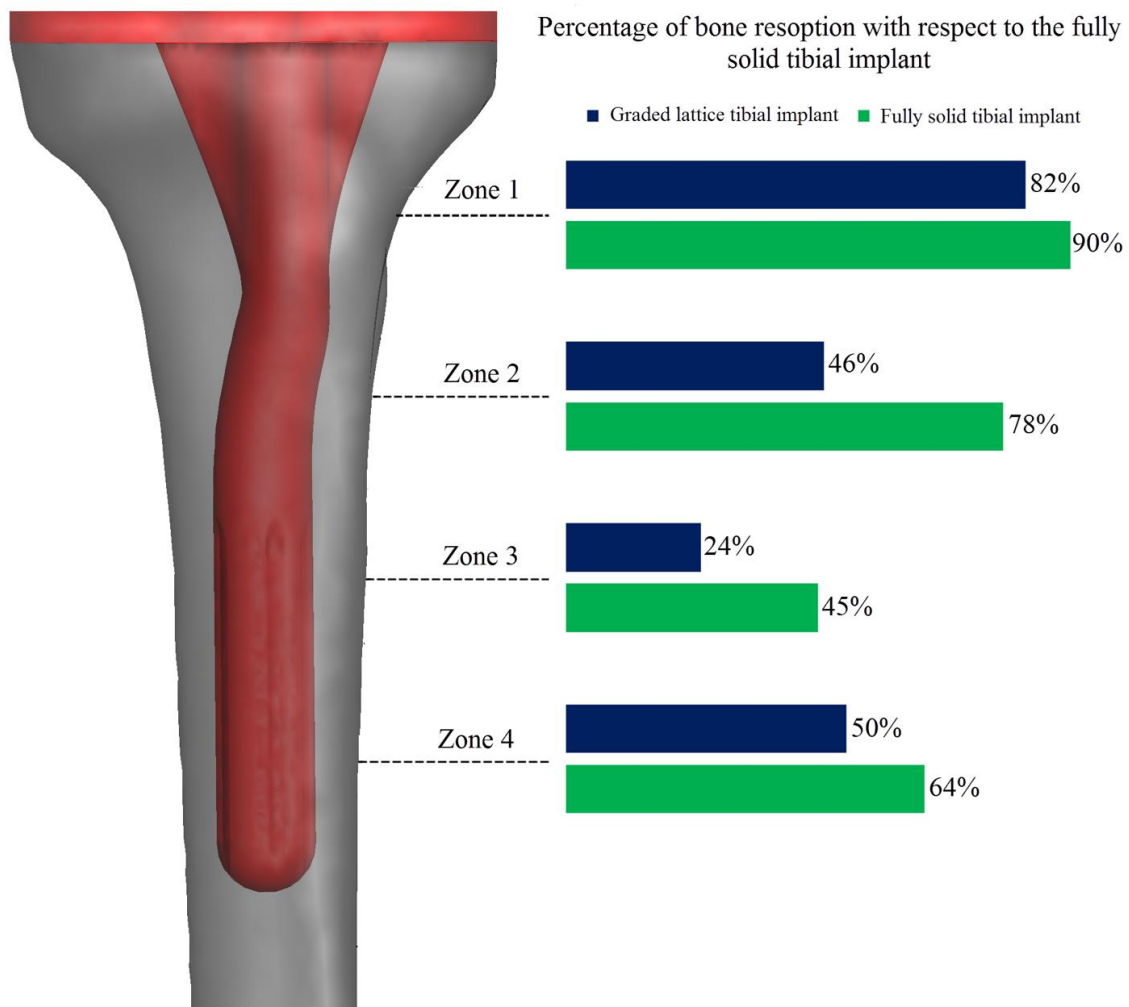


Figure 28: Percentage of bone resorption with respect to a fully solid tibial implant here taken as a baseline for (i) graded cellular implant, and (ii) uniform cellular implant with relative density of 0.6 .

Recent technologies for additive manufacturing (AM), such as electron beam melting (EBM) and selective laser melting (SLM), bring versatile layer-by-layer processes that enable the fabrication of porous materials with tailored cellular architecture [132]. For example, SLM, a powder bed fusion technology, has been used to generate parts with improved mechanical, tribological and corrosion properties [133]. Recent works have demonstrated that AM can successfully build metallic lattice structures including porous implants with complex internal microarchitecture [106, 132, 134-137]. In addition, AM facilitates the fabrication of cellular implants with tailored gradients of porosity and pore morphology that enables bone ingrowth

[138, 139]. A fully porous hip implant featuring a lattice microstructure similar to the one presented in this paper has been recently manufactured through SLM and successfully tested in vitro [55]. Its graded microarchitecture features a minimum strut thickness of 200 $\mu\text{m}$  and a maximum pore size of 800 $\mu\text{m}$ , characteristics that are built through AM and are shared by the knee implant presented in this study [61, 132]. These previous works therefore demonstrate the feasibility of additively manufacturing the knee implant architecture herein reported.

Exploratory in nature, this numeric study holds some limitations that need to be addressed in the future. The first one is that a simplified loading system representing a high body weight has been used to perform the numerical analysis. Although this system of loadings describes the worst-case scenario that can occur during normal daily activities, the real load scenarios that a knee joint undergoes are more complex. In particular, this work did not consider the Varus-Valgus movements that often result in a higher amount of load on the medial compartment than the lateral one. In addition, the magnitude of contact forces varies between ordinary activities and the phase of activity, thus resulting in a complex relationship between the flexion angle, the maximum joint load and the balance of medial to lateral load distribution for different activities. Another aspect that requires further investigation is the sensitivity of the results, e.g. the amount of interface micromotion, to variations in bulk material properties, bone properties, loading conditions and the contact model used at the bone-implant interface.

## **4.5 Conclusions**

This chapter has described the design and computational assessment of a stemmed tibial component with a fully porous stem featuring a tailored lattice architecture. The implant porosity has been tailored to minimize the postoperative bone resorption and end-of-stem pain that can occur following primary and revision TKA. The implant mechanical properties are tuned to locally mimic those of the surrounding bone tissue, thus concomitantly minimize bone resorption and interface micromotion. A lattice Tetrahedron-based cell is used to generate the implant microarchitecture, which has been designed to withstand fatigue failure during the daily cyclic loading conditions a patient would experience. The results demonstrate that this knee implant design attains a substantial reduction of 17  $\mu\text{m}$  and 22  $\mu\text{m}$  in micromotion at the tip of the stem during gait cycle and deep knee bend, respectively. As well, it has been demonstrated that the graded porous implant is extremely stable with micromotion below 50  $\mu\text{m}$  for 95% and 76% of

the implant surface respectively during the gait cycle and deep knee bend. Clinically, this would be expected to prevent the occurrence of end-of-stem pain that is not uncommon after total knee arthroplasty. In addition, this implant design is bone preserving with only 14% of the periprosthetic bone being resorbed with the porous implant. This is significantly less than the 40% bone resorption seen around the identical solid tibial knee implant and could result in a decrease in periprosthetic fractures and improved bone stock at the time of revision surgery.

## Chapter 5: Final Remarks and Future Work

### 5.1 Summary

The stiffness of current orthopedic implants – namely tibial knee implants – is significantly higher than that of the adjacent bone tissue. This stiffness mismatch leads to lower stress being transferred to the surrounding bone, causing bone resorption. The main issue associated with the current knee implants is the end-of-stem pain reported by patients who have received a stemmed tibial knee implant. The cause of this pain has been attributed to the incidence of bone resorption arising from the stiffness mismatch. These complications have substantially reduced the life span of the implants such that numerous patients undergo revision surgery following the primary TKA. Revision surgery is a more complex procedure compared to the primary TKA and has a lower chance of success.

The main focus of this thesis was to develop a new class of orthopaedic tibial knee implants that are able to boost the success rate of knee replacement surgeries. The methodology exploited in this thesis aimed at designing a lattice microstructure for the knee implant such that it features mechanical properties similar to those of bone tissue. Moreover, the methodology accounted for the fatigue strength of the implant, which is what enables the implant to withstand the daily activities a human is subjected to. The material tailoring for the implant's microstructure has been undertaken using topology optimization. The failure analysis and multiscale analysis of the implant was performed using AH theory, which has had its accuracy and computational efficiency proven in the literature.

In Chapter 2, a systematic methodology based on multiscale mechanics and topology optimization was introduced to design the porous microstructure of the implant. The finite element model of the tibia and implant were then created based on the CT data obtained from a 38-year-old male. The available homogenization techniques to analyze the cellular materials were reviewed, and AH theory was selected due to its accuracy. The mathematical formulation of AH theory was described, and it was applied to the characterization of the tetrahedron cell unit used as the building block of the implant microstructure. The effective elastic modulus and yield strength were predicted for the whole range of relative density.

In Chapter 3, the formulation of the topology optimization problem for the implant material tailoring was described. The problem was subjected to a set of constraints on the

average porosity and minimum strut thickness. The multiscale mechanics described in Chapter 2 were integrated to the optimization problem to replace the traditional SIMP method. The closed-form expressions obtained in Chapter 2 were used to relate the elastic constants of the implant microstructure to its density distribution. As a result, the derivative of the objective function was obtained using these expressions.

The methodology described in Chapter 2 was applied to the design of a fully porous tibial knee implant in Chapter 4. The Soderberg fatigue criterion was integrated in the procedure to capture the fatigue safety factor of the implant and ensure a design with an infinite lifespan. It has been observed that for the cellular implant, the amount of bone loss is 25% lower than that of a uniform porosity implant, and 65% lower than that of a fully dense titanium implant. In addition, it has been demonstrated that this knee implant design leads to a reduction of, respectively, 17  $\mu\text{m}$  and 22  $\mu\text{m}$  in micromotion at the tip of the stem during gait cycle and deep knee bend. This reduction in the amount of micromotion offers a highly stable implant with a longer lifespan.

## **5.2 Future work**

The methodology proposed here considers only one unit cell to build the porous microstructure of the implant. There is an infinite number of 3D cell topologies that can be used to tessellate the space. However, many of these unit cells are not suitable to be used as building blocks for orthopedic implants. High porosity, adequate strength, and a large surface area with adequate surface textures are critical criteria that should be considered when selecting a unit cell to design an implant. Based on these criteria, the octet truss lattice unit cell has been identified as an appropriate porous biomaterial with high strength and structural efficiency that can be used to address the limitations of current implants [61]. AH theory can be utilized to characterize the mechanical properties of the octet truss cell for the whole range of relative density. The stiffness properties and fatigue strength of octet cell can be then incorporated into the proposed optimization scheme to design a lattice octet knee implant. Hence, a standard library to select the suitable lattice knee implant can be created [25].

Another underlying assumption associated with the proposed method is related to the AH method. AH assumes periodicity of field quantity at both macro and micro scales. However, periodicity cannot be ensured at the domain boundary and throughout the microstructure due to

the presence of local defects. In addition, to perform the multiscale analysis, the geometry of the unit cell is assumed to be fixed throughout the implant microstructure. However, the implant has been meshed, allowing unit cell rotation and the material properties obtained from AH have been mapped into the elements. This has led to some discrepancies between the actual properties of the implant and those used to design it. To reduce such errors, computational techniques can be applied, such as the boundary layer corrector [140, 141], the multilevel computational approach [142, 143], or the mesh superposition method [144, 145]. Additionally, the local orientation of the elements can be captured by defining local and global coordinate systems for each element separately. In future work, these techniques can be integrated with AH to address the current limitations of AH and thus achieve more accurate results.

Lastly, this thesis was a computational study on the design of a porous tibial knee implant. As a part of future study, the designed porous implant can be manufactured through additive manufacturing. The experimental work can ensure the viability of the proposed methodological approach. The improvement accomplished in the performance and functionality of the knee implants, furthermore, can be accurately observed through experiments.

## References

1. L. Drake, V.W., Mitchell, A., Gray's Anatomy for students. Elsevier/Churchill Livingstone. 2007.
2. Levangie, P.K. and C.C. Norkin, Joint Structure and Function - A comprehensive analysis, ed. t. ed. 2005: Philadelphia: F. A. Davis Company.
3. Darrow, M., The Knee Sourcebook, ed. s. ed. 2002: McGraw-Hill.
4. Darwish, S.M. and A. Al-Samhan, The effect of cement stiffness and tibia tray material on the stresses developed in artificial knee. International Journal of Adhesion and Adhesives, 2008. 28(3): p. 120-125.
5. Robalo, T.J.F., Analysis of bone remodeling in the tibial after total knee prosthesis (Unpublished master's thesis), in Biomedical Engineering Department. 2011, Technical University of Lisbon: Lisbon, Portugal.
6. Liu, Y.L., et al., Anatomic-like polyethylene insert could improve knee kinematics after total knee arthroplasty--a computational assessment. Clin Biomech (Bristol, Avon), 2011. 26(6): p. 612-9.
7. Tortora, G. and .Derrickson. B, Principles of anatomy and physiology, 12<sup>th</sup> ed. 2009, John Wiley & Sons, Inc.
8. Sharpe, K. and D. Bahrman. Hip and femur (2015). Available: <https://clinicalgate.com/hip-and-femur/>
9. The bones of the axial skeleton (2016). Available: <http://slideplayer.com/slide/9432617/>
10. Applied anatomy of the knee (2013). Available: [http://www.orthopaedicmedicineonline.com/downloads/pdf/B9780702031458000879\\_web.pdf](http://www.orthopaedicmedicineonline.com/downloads/pdf/B9780702031458000879_web.pdf)
11. Rath, E., R. Schwarzkopf, and J.C. Richmond, Clinical signs and anatomical correlation of patellar tendinitis. Indian Journal of Orthopaedics, 2010. 44(4): p. 435-437.
12. Robert P. Dunbar, M.J.A.L., MD. Patellar (Kneecap) Fractures (2017). Available: <http://orthoinfo.aaos.org/>
13. Mazzucchelli, L., et al., Cruciate retaining and cruciate substituting ultra-congruent insert. Annals of Translational Medicine, 2016. 4(1): p. 2.
14. Knee: Total Knee Arthroplasty Procedure Overview (2011). Available: <http://www.weberorthopedics.com/knee/knee-procedure.php>.
15. P.F.C Sigma Knee System: Technical Monograph. 2000, England: DePuy International Ltd.
16. Uvehammer, J., J. Kärrholm, and L. Carlsson, Cemented hydroxyapatite fixation of the femoral component of the Freeman-Samuelson total knee replacement. A RADIOSTEREOMETRIC ANALYSIS, 2007. 89-B(1): p. 39-44.
17. Gamelas, J., Artroplastias totais do joelho: estudo comparativo de dois métodos de alinhamento no posicionamento do componente tibial. 2006.

18. P.F.C. Sigma Knee System: Primary cruciate-retaining and cruciate-substituting procedures. 2000, England: DePuy International Ltd.
19. DeAndrade, R., Activities after replacement of the hip or knee. Orthopedic Impairments, Special Ed, 1993.
20. Sibanda N, e.a., Revision rates after primary hip and knee replacement in England between 2003 and 2006. Public Library of Science Medicine, 2008. 5(9): p. 1398–1408.
21. Poirier, N., P. Graf, and F. Dubrana, Mobile-bearing versus fixed-bearing total knee implants. Results of a series of 100 randomised cases after 9years follow-up. Orthopaedics & Traumatology: Surgery & Research, 2015. 101(4): p. S187-S192.
22. Shi, J.F., et al., The effect of polyethylene thickness in fixed- and mobile-bearing total knee replacements. Proc Inst Mech Eng H, 2008. 222(5): p. 657-67.
23. Capella, M., M. Dolfin, and F. Saccia, Mobile bearing and fixed bearing total knee arthroplasty. Annals of Translational Medicine, 2016. 4(7): p. 127.
24. Richard, D. fluoroscope kinematics analysis of fixed versus mobile bearing knee arthroplasty (2012). Available: <https://www.youtube.com/watch?v=s7hJcmmgLdc>
25. Khanoki., S.A., Multiscale mechanics and multiobjective optimization of cellular hip implants with variable stiffness. 2013, Doctor of Philosophy: McGill University.
26. Hacking, S.A., et al., Acid-etched microtexture for enhancement of bone growth into porous-coated implants. The Journal of Bone & Joint Surgery, 2003. 85(8): p. 1182-9.
27. Kieswetter, K., et al., Surface roughness modulates the local production of growth factors and cytokines by osteoblast-like MG-63 cells. Journal of Biomedical Materials Research Part A 1996. 32(1): p. 55-63.
28. Yuan, H., et al., A preliminary study on osteoinduction of two kinds of calcium phosphate ceramics. Biomaterials, 1999. 20(19): p. 1799-1806.
29. Bobyn, J.D., et al., The optimum pore size for the fixation of porous-surfaced metal implants by the ingrowth of bone. Clinical Orthopaedics and Related Research, 1980(150): p. 263-70.
30. Bragdon, C.R., et al., Biologic fixation of total hip implants. Insights gained from a series of canine studies. Journal of Bone & Joint Surgery, 2004. 86-A Suppl 2: p. 105-17.
31. Mabry, T.M. and A.D. Hanssen, The role of stems and augments for bone loss in revision knee arthroplasty. Journal of Arthroplasty, 2007. 22(4 Suppl 1): p. 56-60.
32. Sparmann, M., et al., Positioning of total knee arthroplasty with and without navigation support. A prospective, randomised study. Journal of Bone & Joint Surgery, 2003. 85(6): p. 830-5.
33. Completo, A., et al., Biomechanical evaluation of proximal tibia behaviour with the use of femoral stems in revision TKA: an in vitro and finite element analysis. Journal of Clinical Biomechanics 2010. 25(2): p. 159-65.
34. Vichinsky, E.P., et al., The perioperative complication rate of orthopedic surgery in sickle cell disease: report of the National Sickle Cell Surgery Study Group. American Journal of Hematology 1999. 62(3): p. 129-38.



35. Azodi, O.S., et al., High body mass index is associated with increased risk of implant dislocation following primary total hip replacement: 2,106 patients followed for up to 8 years. *Acta Orthopaedica*, 2008. 79(1): p. 141-147.
36. Carr, B.C. and T. Goswami, Knee implants – Review of models and biomechanics. *Materials & Design*, 2009. 30(2): p. 398-413.
37. Mihalko, W.M. and L.A. Whiteside, Stem pain after cementless revision total knee arthroplasty. *Journal of Surgical Orthopaedic Advances*, 2015. 24(2): p. 137-9.
38. Glenn, J.C., et al., Tibia pain at end of stem with stemmed revision total knee arthroplasty: treatment with cortical strut graft technique. *Journal of Arthroplasty*, 2010. 25(3): p. 497 e1-5.
39. Jasty, M., et al., The initiation of failure in cemented femoral components of hip arthroplasties. *The Journal of Bone & Joint Surgery*, 1991. 73(4): p. 551-8.
40. Rakotomanana, L.R., et al., Comparison of tibial fixations in total knee arthroplasty: an evaluation of stress distribution and interface micromotions. *The Knee*, 1994. 1(2): p. 91-99.
41. Barrack, R.L., et al., The effect of stem design on end-of-stem pain in revision total knee arthroplasty. *Journal of Arthroplasty*, 2004. 19(7 Suppl 2): p. 119-24.
42. Haas, S.B., et al., Revision total knee arthroplasty with use of modular components with stems inserted without cement. *The Journal of Bone & Joint Surgery*, 1995. 77(11): p. 1700-7.
43. Barrack, R.L., et al., Pain at the end of the stem after revision total knee arthroplasty. *Clinical Orthopaedics and Related Research*, 1999(367): p. 216-25.
44. Completo, A., et al., A new press-fit stem concept to reduce the risk of end-of-stem pain at revision TKA: a pre-clinical study. *Knee*, 2012. 19(5): p. 537-42.
45. Bahraminasab, M., et al., Aseptic loosening of femoral components – Materials engineering and design considerations. *Materials & Design*, 2013. 44: p. 155-163.
46. Bahraminasab, M., et al., Multi-objective design optimization of functionally graded material for the femoral component of a total knee replacement. *Materials & Design*, 2014. 53: p. 159-173.
47. Completo, A., et al., Biomechanical evaluation of proximal tibia behaviour with the use of femoral stems in revision TKA: An in vitro and finite element analysis. *Clinical Biomechanics*, 2010. 25(2): p. 159-165.
48. Greenwald, A.S. and C.S. Heim, Mobile-bearing knee systems: ultra-high molecular weight polyethylene wear and design issues. *Instructional Course Lectures* 2005. 54: p. 195-205.
49. McEwen, H.M., et al., The influence of design, materials and kinematics on the in vitro wear of total knee replacements. *Journal of Biomechanics*, 2005. 38(2): p. 357-65.
50. Bureau, M.N., et al., Biomimetic Polymer Composites for Orthopedic Implants.

51. Van Lenthe, G.H., M.C. de Waal Malefijt, and R. Huiskes, Stress shielding after total knee replacement may cause bone resorption in the distal femur. *Journal of Bone & Joint Surgery*, 1997. 79(1): p. 117-22.
52. Arabnejad Khanoki, S. and D. Pasini, Multiscale design and multiobjective optimization of orthopedic hip implants with functionally graded cellular material. *Journal of Biomechanical Engineering* 2012. 134(3): p. 031004.
53. Arabnejad Khanoki, S. and D. Pasini, Fatigue design of a mechanically biocompatible lattice for a proof-of-concept femoral stem. *Journal of the Mechanical Behavior of Biomedical Materials*, 2013. 22: p. 65-83.
54. Arabnejad Khanoki, S. and D. Pasini, The Fatigue Design of a Bone Preserving Hip Implant With Functionally Graded Cellular Material. *Journal of Medical Devices*, 2013. 7(2): p. 020907-020907.
55. Arabnejad, S., et al., Fully porous 3D printed titanium femoral stem to reduce stress-shielding following total hip arthroplasty. *Journal of Orthopaedic Research* 2017. 35 (8): p. 1774–1783.
56. Au, A.G., et al., Contribution of loading conditions and material properties to stress shielding near the tibial component of total knee replacements. *Journal of Biomechanics*, 2007. 40(6): p. 1410-6.
57. Enab, T.A., A comparative study of the performance of metallic and FGM tibia tray components in total knee replacement joints. *Computational Materials Science*, 2012. 53(1): p. 94-100.
58. Bobyn, J.D., et al., Clinical validation of a structural porous tantalum biomaterial for adult reconstruction. *Journal of Bone & Joint Surgery*, 2004. 86-A Suppl 2: p. 123-9.
59. Kuiper, J. and H.R. Huiskes, Numerical optimization of hip-prosthetic stem material. 1992, Books and Journals International: Swansea.
60. Kuiper, J.H. and R. Huiskes, Mathematical optimization of elastic properties: application to cementless hip stem design. *Journal of Biomechanical Engineering* 1997. 119(2): p. 166-74.
61. Arabnejad, S., et al., High-strength porous biomaterials for bone replacement: A strategy to assess the interplay between cell morphology, mechanical properties, bone ingrowth and manufacturing constraints. *Acta Biomaterialia* 2016. 30: p. 345-56.
62. Bendsøe, M.P. and N. Kikuchi, Generating optimal topologies in structural design using a homogenization method. *Computer Methods in Applied Mechanics and Engineering*, 1988. 71(2): p. 197-224.
63. Bendsøe, M.P. and O. Sigmund, *Topology Optimization: Theory, Methods, and Applications*, B. Springer-Verlag, Editor. 2003.
64. DÍAAZ, A.R. and N. Kikuchi, Solutions to shape and topology eigenvalue optimization problems using a homogenization method. *International Journal for Numerical Methods in Engineering*, 1992. 35(7): p. 1487-1502.

65. Guedes, J. and N. Kikuchi, Preprocessing and postprocessing for materials based on the homogenization method with adaptive finite element methods. *Computer Methods in Applied Mechanics and Engineering*, 1990. 83(2): p. 143-198.
66. Hassani, B. and E. Hinton, A review of homogenization and topology optimization III—topology optimization using optimality criteria. *Computers & Structures*, 1998. 69(6): p. 739-756.
67. Suzuki, K. and N. Kikuchi, A homogenization method for shape and topology optimization. *Computer Methods in Applied Mechanics and Engineering*, 1991. 93(3): p. 291-318.
68. Coelho, P.G., et al., Parallel computing techniques applied to the simultaneous design of structure and material. *Advances in Engineering Software*, 2011. 42(5): p. 219-227.
69. Coelho, P.G., et al., A hierarchical model for concurrent material and topology optimisation of three-dimensional structures. *Structural and Multidisciplinary Optimization*, 2008. 35(2): p. 107-115.
70. Fang, Z., B. Starly, and W. Sun, Computer-aided characterization for effective mechanical properties of porous tissue scaffolds. *Computer-Aided Design*, 2005. 37(1): p. 65-72.
71. Hassani, B. and E. Hinton, A review of homogenization and topology optimization I—homogenization theory for media with periodic structure. *Computers & Structures*, 1998. 69(6): p. 707-717.
72. Hassani, B. and E. Hinton, A Review of Homogenization and Topology Optimization I I- Analytical and Numerical Solution of Homogenization Equations. *Journal of Computers & Structures* 1998. 69(6): p. 719-738.
73. Zienkiewicz, O.C. and R.L. Taylor, in *The Finite Element Method for Solid and Structural Mechanics (Sixth Edition)*. 2005, Butterworth-Heinemann: Oxford. p. i.
74. Baca, V., et al., Comparison of an inhomogeneous orthotropic and isotropic material models used for FE analyses. *Medical Engineering & Physics*, 2008. 30(7): p. 924-930.
75. Peng, L., et al., Comparison of isotropic and orthotropic material property assignments on femoral finite element models under two loading conditions. *Journal of Medical Engineering & Physics* 2006. 28(3): p. 227-33.
76. Austman, R.L., et al., The effect of the density–modulus relationship selected to apply material properties in a finite element model of long bone. *Journal of Biomechanics*, 2008. 41(15): p. 3171-3176.
77. Peng, L., et al., Comparison of isotropic and orthotropic material property assignments on femoral finite element models under two loading conditions. *Medical Engineering & Physics*, 2006. 28(3): p. 227-233.
78. Viceconti, M., et al., Large-sliding contact elements accurately predict levels of bone-implant micromotion relevant to osseointegration. *Journal of Biomechanics*, 2000. 33(12): p. 1611-8.

79. Hipp, J.A., et al., Finite element model of implants in bone: interfacial assumptions. Rensselaer Polytechnic Institute, Troy, NY, U.S.A. .
80. Bergmann, G., et al., Standardized Loads Acting in Knee Implants. PLoS ONE, 2014. 9(1): p. e86035.
81. Heinlein, B., et al., ESB Clinical Biomechanics Award 2008: Complete data of total knee replacement loading for level walking and stair climbing measured in vivo with a follow-up of 6-10 months. Clin Biomech (Bristol, Avon), 2009. 24(4): p. 315-26.
82. Kutzner, I., et al., Loading of the knee joint during activities of daily living measured in vivo in five subjects. Journal of Biomechanics, 2010. 43(11): p. 2164-73.
83. Arabnejad, S. and D. Pasini, Mechanical properties of lattice materials via asymptotic homogenization and comparison with alternative homogenization methods. International Journal of Mechanical Sciences, 2013. 77: p. 249-262.
84. Banerjee, S. and A. Bhaskar, The applicability of the effective medium theory to the dynamics of cellular beams. International Journal of Mechanical Sciences, 2009. 51(8): p. 598-608.
85. Gibson, L.J. and M.F. Ashby, Cellular Solids: Structure and Properties, C. Cambridge University Press, UK, Editor. 1999.
86. Kumar, R.S. and D.L. McDowell, Multifunctional design of two-dimensional cellular materials with tailored mesostructure. International Journal of Solids and Structures, 2009. 46(14–15): p. 2871-2885.
87. Christensen, R.M., Mechanics of cellular and other low-density materials. International Journal of Solids and Structures, 2000. 37(1–2): p. 93-104.
88. Masters, I.G. and K.E. Evans, Models for the elastic deformation of honeycombs. Composite Structures, 1996. 35(4): p. 403-422.
89. Wang, A.J. and D.L. McDowell, In-Plane Stiffness and Yield Strength of Periodic Metal Honeycombs. Journal of Engineering Materials and Technology, 2004. 126(2): p. 137-156.
90. Gibson, L.J., et al., The Mechanics of Two-Dimensional Cellular Materials. Proceedings of the Royal Society of London. A. Mathematical and Physical Sciences, 1982. 382(1782): p. 25-42.
91. Elsayed, M.S.A. and D. Pasini, Analysis of the elastostatic specific stiffness of 2D stretching-dominated lattice materials. Mechanics of Materials, 2010. 42(7): p. 709-725.
92. Kalamkarov, A.L., I.V. Andrianov, and V.V. Danishevs'kyy, Asymptotic Homogenization of Composite Materials and Structures. Applied Mechanics Reviews, 2009. 62(3): p. 030802-030802-20.
93. Bendsøe, M.P., Optimal shape design as a material distribution problem. Structural optimization, 1989. 1(4): p. 193-202.
94. Sigmund, O., Materials with prescribed constitutive parameters: An inverse homogenization problem. International Journal of Solids and Structures, 1994. 31(17): p. 2313-2329.

95. Guinovart-Díaz, R., et al., Modeling of elastic transversely isotropic composite using the asymptotic homogenization method. Some comparisons with other models. *Materials Letters*, 2002. 56(6): p. 889-894.
96. Guinovart-Díaz, R., et al., Asymptotic Analysis of Linear Thermoelastic Properties of Fiber Composites. *Journal of Thermoplastic Composite Materials*, 2007. 20(4): p. 389-410.
97. Takano, N., et al., Microstructure-based deep-drawing simulation of knitted fabric reinforced thermoplastics by homogenization theory. *International Journal of Solids and Structures*, 2001. 38(36–37): p. 6333-6356.
98. Takano, N., et al., Microstructure-based stress analysis and evaluation for porous ceramics by homogenization method with digital image-based modeling. *International Journal of Solids and Structures*, 2003. 40(5): p. 1225-1242.
99. Jansson, S., Homogenized nonlinear constitutive properties and local stress concentrations for composites with periodic internal structure. *International Journal of Solids and Structures*, 1992. 29(17): p. 2181-2200.
100. Matsui, K., K. Terada, and K. Yuge, Two-scale finite element analysis of heterogeneous solids with periodic microstructures. *Computers & Structures*, 2004. 82(7–8): p. 593-606.
101. Masoumi Khalil Abad, E., S. Arabnejad Khanoki, and D. Pasini, Fatigue design of lattice materials via computational mechanics: Application to lattices with smooth transitions in cell geometry. *International Journal of Fatigue*, 2013. 47: p. 126-136.
102. Hollister, S.J. and N. Kikuchi, A comparison of homogenization and standard mechanics analyses for periodic porous composites. *Computational Mechanics*, 1992. 10(2): p. 73-95.
103. Hassani, B., A direct method to derive the boundary conditions of the homogenization equation for symmetric cells. *Communications in Numerical Methods in Engineering*, 1996. 12(3): p. 185-196.
104. Parthasarathy, J., et al., Mechanical evaluation of porous titanium (Ti6Al4V) structures with electron beam melting (EBM). *Journal of the Mechanical Behavior of Biomedical Materials*, 2010. 3(3): p. 249-259.
105. Wycisk E, E.C., Siddique S, Walter L. F., High cycle fatigue (HCF) performance of Ti-6Al- 4V alloy processed by selective laser melting. *Advanced Materials Research: Trans Tech Publ*, 2013: p. 134-139.
106. Liu, L., et al., Elastic and failure response of imperfect three-dimensional metallic lattices: the role of geometric defects induced by Selective Laser Melting. *Journal of the Mechanics and Physics of Solids*, 2017. 107: p. 160-184.
107. Bendsøe, M. and O. Sigmund, *Topology optimization: theory, method and applications*. 2003, Springer.
108. Lagaros, N.D. and M. Papadrakakis, *Engineering and Applied Sciences Optimization: Dedicated to the Memory of Professor M.G. Karlaftis*. 2015: Springer International Publishing.

109. Gogarty, E., Hierarchical topology optimization for bone tissue scaffold, in Department of Mechanical Engineering. 2014, McGill University.
110. Kohn, R.V. and G. Strang, Optimal design and relaxation of variational problems, I. Communications on Pure and Applied Mathematics, 1986. 39(1): p. 113-137.
111. Kohn, R.V. and G. Strang, Optimal design and relaxation of variational problems, II. Communications on Pure and Applied Mathematics, 1986. 39(2): p. 139-182.
112. Kohn, R.V. and G. Strang, Optimal design and relaxation of variational problems, III. Communications on Pure and Applied Mathematics, 1986. 39(3): p. 353-377.
113. Zhou, M. and G.I.N. Rozvany, Second World Congress on Computational Mechanics The COC algorithm, Part II: Topological, geometrical and generalized shape optimization. Computer Methods in Applied Mechanics and Engineering, 1991. 89(1): p. 309-336.
114. Allaire, G., Shape optimization by the homogenization method, Springer, Editor. 2001: New York.
115. Bendsøe, M., Optimization of structural topology shape and material, Springer, Editor. 1995: New York.
116. Haber, R.B., C.S. Jog, and M.P. Bendsøe, A new approach to variable-topology shape design using a constraint on perimeter. Structural optimization, 1996. 11(1): p. 1-12.
117. Jog, C.S., Topology design of structures using a dual algorithm and a constraint on the perimeter. International Journal for Numerical Methods in Engineering, 2002. 54(7): p. 1007-1019.
118. Cadman, J.E., et al., On design of multi-functional microstructural materials. Journal of Materials Science, 2013. 48(1): p. 51-66.
119. Avinash Shukla, A.M., Review of optimality criterion approach scope, limitation and development in topology optimization. International Journal of Advances in Engineering & Technology, 2013. Vol. 6(Issue 4): p. 1886-1889.
120. Svanberg, K., The method of moving asymptotes—a new method for structural optimization. International Journal for Numerical Methods in Engineering, 1987. 24(2): p. 359-373.
121. Svanberg, K., The Method of Moving Asymptotes (MMA) with Some Extensions, in Optimization of Large Structural Systems, G.I.N. Rozvany, Editor. 1993, Springer Netherlands: Dordrecht. p. 555-566.
122. Hsu, M.-H., Integrating 2-D and 3-D topology and shape optimization using the density contour approach. 2003, Yuan Ze University.
123. Sigmund, O. and J. Petersson, Numerical instabilities in topology optimization: A survey on procedures dealing with checkerboards, mesh-dependencies and local minima. Structural optimization, 1998. 16(1): p. 68-75.
124. Liu, K. and A. Tovar, An efficient 3D topology optimization code written in Matlab. Structural and Multidisciplinary Optimization, 2014. 50(6): p. 1175-1196.

125. Ridzwan M, S.S., Hassan A, Shokri A, Ibrahim MM, Problem of stress shielding and improvement to the hip implant designs: a review. *Journal of Medical Science*, 2007. 7: p. 460-467.
126. Logan, D.L., *A First Course in the Finite Element Method Using Algor*. 2000: Brooks/Cole Publishing Co. 864.
127. ASTM F1800-12, Standard Practice for Cyclic Fatigue Testing of Metal Tibial Tray Components of Total Knee Joint Replacements. 2012, West Conshohocken, PA.
128. Small, S.R., et al., Micromotion at the tibial plateau in primary and revision total knee arthroplasty: fixed versus rotating platform designs. *Bone & Joint Research*, 2016. 5(4): p. 122-129.
129. Conlisk, N., et al., The influence of stem length and fixation on initial femoral component stability in revision total knee replacement. *Bone & Joint Research*, 2012. 1(11): p. 281-288.
130. Chong, D.Y., U.N. Hansen, and A.A. Amis, Analysis of bone-prosthesis interface micromotion for cementless tibial prosthesis fixation and the influence of loading conditions. *Journal of Biomechanics*, 2010. 43(6): p. 1074-80.
131. Ebrahimi, H., et al., Biomechanical properties of an intact, injured, repaired, and healed femur: an experimental and computational study. *Journal of the Mechanical Behavior of Biomedical Materials* 2012. 16: p. 121-35.
132. Melancon, D., et al., Mechanical characterization of structurally porous biomaterials built via additive manufacturing: experiments, predictive models, and design maps for load-bearing bone replacement implants. *Acta Biomaterialia*, 2017.
133. Konda Gokuldoss, P., S. Kolla, and J. Eckert, Additive Manufacturing Processes: Selective Laser Melting, Electron Beam Melting and Binder Jetting—Selection Guidelines. *Materials*, 2017. 10(6): p. 672.
134. Vaezi, M., et al., Multiple material additive manufacturing – Part 1: a review. *Virtual and Physical Prototyping*, 2013. 8(1): p. 19-50.
135. Balla, V.K., et al., Porous Tantalum Structures for Bone Implants: Fabrication, Mechanical and In vitro Biological Properties. *Acta biomaterialia*, 2010. 6(8): p. 3349-3359.
136. Moiduddin, K., et al., Structural and mechanical characterization of custom design cranial implant created using additive manufacturing. *Electronic Journal of Biotechnology*, 2017. 29(Supplement C): p. 22-31.
137. Tunchel, S., et al., 3D Printing/Additive Manufacturing Single Titanium Dental Implants: A Prospective Multicenter Study with 3 Years of Follow-Up. *International Journal of Dentistry*, 2016. 2016: p. 8590971.
138. Sobral, J.M., et al., Three-dimensional plotted scaffolds with controlled pore size gradients: Effect of scaffold geometry on mechanical performance and cell seeding efficiency. *Acta Biomaterialia*, 2011. 7(3): p. 1009-18.

139. Khoda, A.K., I.T. Ozbolat, and B. Koc, Engineered tissue scaffolds with variational porous architecture. *Journal of Biomechanical Engineering* 2011. 133(1): p. 011001.
140. M. Lefik, B.S., FE modelling of a boundary layer corrector for composites using the homogenization theory. *Engineering Computations*, 1996. Vol. 13 (Issue: 6): p. 31-42.
141. Dumontet, H., Study of a boundary layer problem in elastic composite materials. *Mathematical Modelling and Numerical Analysis*, 1986. 20(2): p. 265-286.
142. Ghosh, S., K. Lee, and P. Raghavan, A multi-level computational model for multi-scale damage analysis in composite and porous materials. *International Journal of Solids and Structures*, 2001. 38(14): p. 2335-2385.
143. Raghavan, P. and S. Ghosh, Concurrent multi-scale analysis of elastic composites by a multi-level computational model. *Computer Methods in Applied Mechanics and Engineering*, 2004. 193(6–8): p. 497-538.
144. Takano, N. and Y. Okuno, Three-scale finite element analysis of heterogeneous media by asymptotic homogenization and mesh superposition methods. *International Journal of Solids and Structures*, 2004. 41(15): p. 4121-4135.
145. Takano, N., M. Zako, and Y. Okuno, Multi-Scale Finite Element Analysis for Joint Members of Heterogeneous Dissimilar Materials with Interface Crack. *Journal of the Society of Materials Science, Japan*, 2003. 52(8): p. 952-957.



## Appendices

### Appendix A: Assigning bone material properties using computed tomography (CT) data

The heterogeneous material properties of the tibia are captured through computed tomography (CT) data obtained from a 38 year old male , provided by the Visible Human project (United States National Library of Medicine, Bethesda, MD). The radiographic density of the CT images quantified as Hounsfield Unit (HU) is used to calculate the local properties of the tibia. Since the relationship between the HU and bone density is monotonic, a linear relationship between the bone apparent density and the HU is adopted as shown in **Error! Reference source not found.** A.1 [75]. The bone apparent density represents the density of solid bone excluding the density of the fluid mass, namely the density of blood. On the other hand, the bone effective density accounts for the fluid mass. At regions where there is no bone, the effective density would be about 1024 kg/m<sup>3</sup>, which represents the density of blood. However at these regions, the apparent density and the HU value are zero.

To obtain the mechanical properties of the tibia, the apparent density for each element of the finite element model is determined from the HU value measured from the CT data ranging from 0 HU to 1567 HU. This ensures that the density of the fluid has no contribution to the mechanical properties of the tibia. The maximum value of HU corresponds to the densest region of the cortical bone with an apparent density of 2000 kg/m<sup>3</sup>. The Young modulus of the tibia is then obtained using the relation

$$\begin{cases} E = 1904 \rho^{1.64} & \rho < 0.95 \\ E = 2065 \rho^{3.09} & 0.95 < \rho \end{cases}, \quad \nu = 0.3 \quad (\text{A.1})$$

where E is the elastic modulus of bone, and  $\nu$  is its Poisson's ratio. The properties are assumed to be isotropic, a simplification that does not lead to a considerable difference from the results that consider bone as orthotropic [74, 75]. This assumption contributes also to reduce the computational cost.

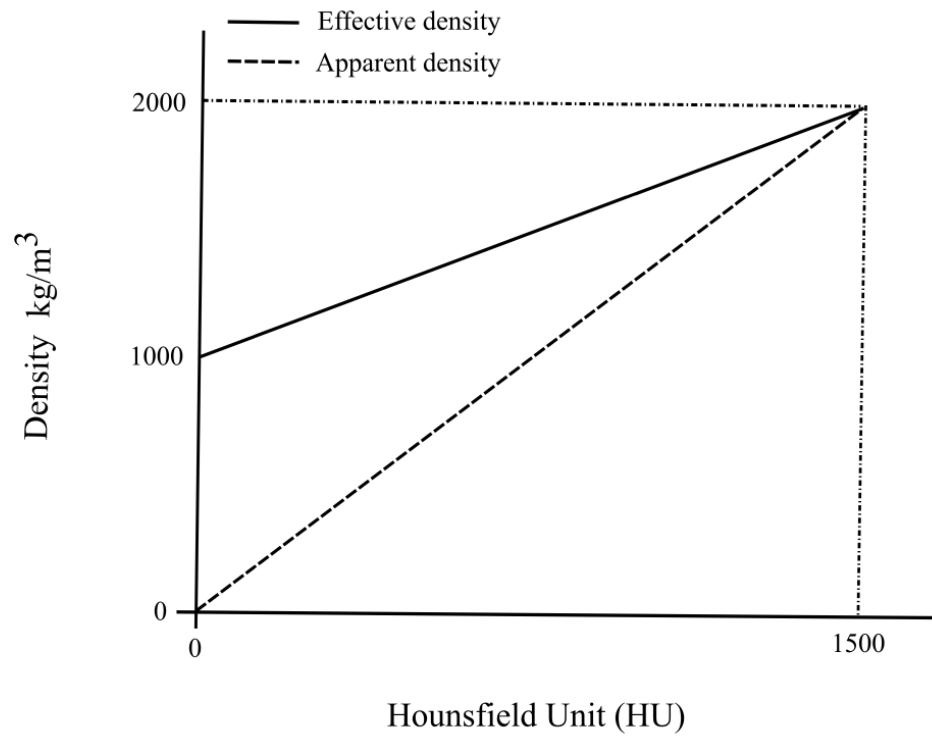


Figure A.1: Linear relationship between Hounsfield number and both effective density and apparent density.

## Appendix B: Filter density function

Initial formulations of topology optimization problems generally yield instabilities in the optimal solutions that in turn affect result accuracy. A continuous density distribution is an asset for the implant strength while a discontinuous density distribution in the implant microstructure leads to stress concentration and compromise the implant strength thus increasing the probability of local failure. To avoid binary results (black and white patterns) for the density distribution, we use the following filter density function [123], to obtain the mechanical properties of each finite element mesh:

$$\tilde{x}_i = \frac{\sum_{j \in N_i} H_{ij} v_j x_j}{\sum_{j \in N_i} H_{ij} v_j} \quad (\text{B.1})$$

wherein,  $N_i$  corresponds to neighborhood elements of element  $i$ , with volume of  $v_i$ .

$H_{ij}$  is a weight factor matrix determined as follows:

$$H_{ij} = R - \text{dist}(i, j) \quad (\text{B.2})$$

where  $R$  is the size of the neighbourhood that is referred to the filter size and  $\text{dist}(i, j)$  is the distance between the element  $i$  and the center of the element  $j$ . The neighborhood of an element is defined as

$$N_i = \{j : \text{dist}(i, j) \leq R\} \quad (\text{B.3})$$

## Appendix C: Convergence plot of the topology optimization scheme

As described in chapter 3, a density-based topology optimization is used in this thesis to optimally tailor the density gradients of the implant. To ensure solution convergence, we resort to the optimality criteria methods [115], in particular here we use the standard optimality criterion based on the Lagrangian function that benefits from knowledge on the physics and mechanics of the problem [119]. This method requires the calculation of the derivative of the objective function along with the derivative of the design constraints to update the design variables based on the initial guess [119].

In this work, the derivative of the implant compliance - obtained as described in chapter 3 - is used with the standard optimality criterion to find the optimum density distribution. As per the initial guess, a uniform relative density of 0.5 is assigned to the implant and the total strain energy of the implant is calculated. The optimization continues until the difference between two successive iterations is below 1%. As shown in the figure below, the objective function converges within 31 iterations.

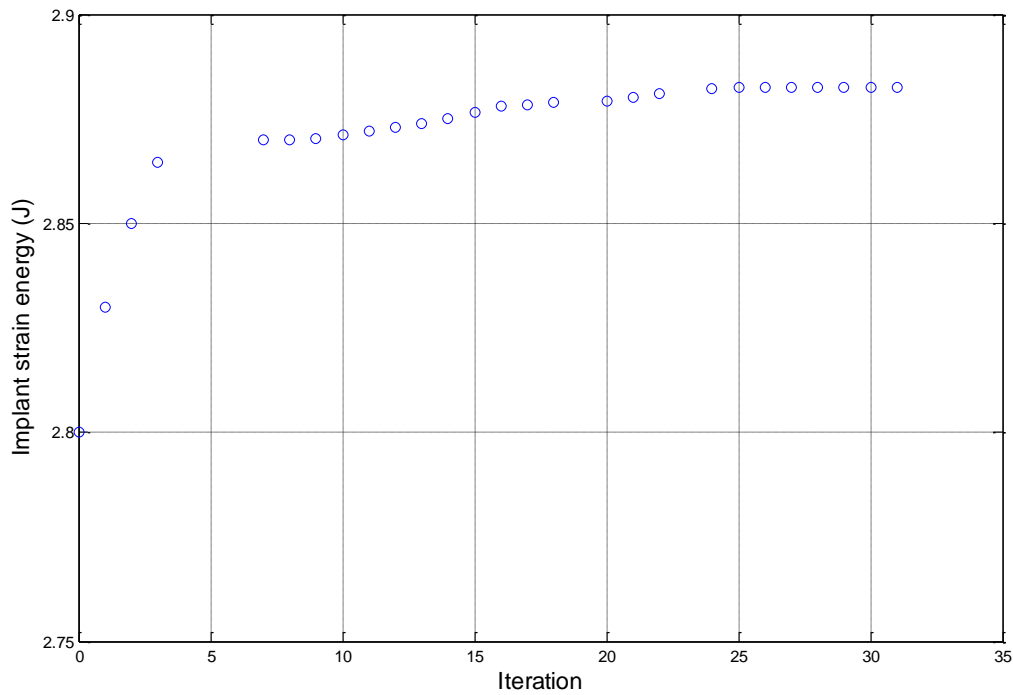


Figure C.1: The convergence plot of the topology optimization scheme.